

# Analysis of Signal Yield and Branching Ratio of

$$D^{*0} \rightarrow D^0 \gamma, D^0 \rightarrow K^- \pi^+$$



**Arnab Das, 20PH05005**

Supervisor: Dr. Seema Bahinipati  
*Department of Physics, IIT Bhubhaneswar*

# Contents

<b>1</b>	<b>A Brief Note on Particles</b>	<b>1</b>
1.1	Introduction . . . . .	1
1.2	Introduction to Elementary Particles . . . . .	1
1.2.1	Discovery of Electron . . . . .	1
1.2.2	Discovery of Proton . . . . .	2
1.2.3	Discovery of Neutron . . . . .	2
1.2.4	Discovery of the Photon . . . . .	2
1.3	Introduction to the family of Quarks and Leptons . . . . .	3
1.4	Introduction to $D^{*0}$ . . . . .	5
<b>2</b>	<b>Historical Background</b>	<b>7</b>
2.1	Motivation and Theory . . . . .	7
<b>3</b>	<b>The Belle II Experiment</b>	<b>9</b>
3.1	SuperKEKB and Belle II Detector . . . . .	9
3.2	The Physics program of Belle II . . . . .	11
<b>4</b>	<b>Software Tools for Analysis</b>	<b>13</b>
4.1	ROOT . . . . .	13
4.2	RooFit . . . . .	14
4.2.1	Mathematical Model . . . . .	14
4.2.2	Design . . . . .	15
4.3	Basf2 . . . . .	15
4.3.1	Modules and Path . . . . .	15
4.3.2	Steering Script . . . . .	16
<b>5</b>	<b>Analysis of the decay channel of <math>D^{*0}</math></b>	<b>17</b>
5.1	Reconstruction . . . . .	17
5.1.1	Tracking . . . . .	18
5.1.2	Particle Identification . . . . .	19
5.1.3	Particle Reconstruction and Variable Declaration . . . . .	20

5.2	Observation from Histograms . . . . .	22
5.2.1	Mass of $\mathbf{D}^0$ . . . . .	22
5.2.2	Mass of $\mathbf{D}^{*0}$ . . . . .	23
5.2.3	Mass difference between $D^{*0}$ and $D^0$ . . . . .	25
<b>6</b>	<b>Optimization of the reconstructed decay channel of <math>\mathbf{D}^{*0}</math></b>	<b>27</b>
6.1	Cut and Count Method . . . . .	27
6.2	Variable Selection . . . . .	28
6.2.1	Kaons( $K^-$ ) . . . . .	29
6.2.2	Pions( $\pi^+$ ) . . . . .	30
6.2.3	gamma( $\gamma$ ) . . . . .	31
6.2.4	gamma( $\gamma$ ) in forward region(clusterReg==1) . . . . .	32
6.2.5	gamma( $\gamma$ ) in barrel region(clusterReg==2) . . . . .	34
6.2.6	gamma( $\gamma$ ) in backward region(clusterReg==3) . . . . .	35
6.2.7	$D^0$ meson . . . . .	36
6.3	First Optimisation . . . . .	39
6.4	Second Optimisation . . . . .	40
6.5	Third Optimisation . . . . .	42
6.6	Fourth Optimisation . . . . .	45
6.7	Fifth Optimisation . . . . .	47
6.8	Result after Optimisation . . . . .	49
<b>7</b>	<b>Fitting of <math>\Delta M</math> after optimisation</b>	<b>51</b>
7.1	Signal Fitting . . . . .	51
7.1.1	Crystal Ball Function . . . . .	53
7.2	Background Fitting . . . . .	53
7.3	Total Fitting . . . . .	55

# Chapter 1

## A Brief Note on Particles

### 1.1 Introduction

Elementary particle physics helps us to get an idea about the composition of matter. It shows us the most fundamental particles that form most of the matter that we see in our day to day life. Before going deep into the analysis and decay of  $D^{*0}$  and  $D_s^{*+}$  let us look into the elementary particles and how do we get our particle of interest.

### 1.2 Introduction to Elementary Particles

Beginning the talk on particle physics we must always ask the question, "What is matter made of on the most fundamental level?". The answer to this is really remarkable if we look in detail. We see that the subatomic particles that make up the huge chunks of matter are mostly hollow with vast empty spaces and tiny chunks here and there. These tiny chunks can be electrons, protons, neutrons, pi mesons, etc. The most fascinating thing about these particles is that they are identical to itself. Thus one cannot distinguish between two electrons just by putting some identification number. If we see one electron, all the other electrons will be similar. Thus the first job here would be to introduce various kinds of elementary particles and their properties.[16]

#### 1.2.1 Discovery of Electron

Starting to talk about elementary particles one must start with electron which can be produced most easily. Although in today's world producing an electron is not a big deal yet it took scientists many years to pinpoint an electron. It was in 1897 when J.J.Thomson discovered electron from cathode rays by using a perforated anode. Thomson at first called them corpuscles but later the word electron was applied to particles themselves. Thomson proposed that these electrons were essential constituents of atoms and it was

really the case as observed from later experiments. But as the atom is electrically neutral and its mass was much heavier than the mass of electrons constituting it, there must be some massive particle which has charge opposite to that of electrons and are in equal number as those of electrons. This paved the way to the discovery of protons by Ernest Rutherford.[16]

### **1.2.2 Discovery of Proton**

It took more than 10 years to find a particle with charge opposite to that of electron and having mass which constitutes the atom. It was in 1911 that Rutherford by his famous  $\alpha$ -particle scattering experiment proved the existence of the nucleus where all the positive charge of the atom are concentrated. Rutherford concluded that the  $\alpha$ -particles encountered something very small but heavy particle that made them bounce back towards their incident direction. Thus this positively charged particle must be present at the center of the atom with all the mass concentrated there. Rutherford named the nucleus of the lightest atom(hydrogen) as proton. Unfortunately, the next heavier atom after hydrogen(i.e., helium) although carried two protons and two electrons, its mass was calculated to be four times the mass of a single proton. This led to the discovery of another subatomic particle called neutron.[16]

### **1.2.3 Discovery of Neutron**

The mass problem of atoms remained a dilemma for many years. Scientists had to look for a particle which has mass similar to that of protons but should be electrically neutral. It was in 1932 that James Chadwick discovered a particle that was neutral but had mass comparable to that of the proton. This particle later came to be called the neutron. It was concluded that helium nucleus had two protons and two neutrons in total. Afterwards it was observed that the number of neutrons is flexible and the same atom may come in several different isotopes, having the number of protons similar but differing only in the number of neutrons.[16]

### **1.2.4 Discovery of the Photon**

The first contribution towards the idea of photon was given by Planck in 1900 while trying to explain the blackbody radiation. He was the first to quantize electromagnetic radiation(radiation came in small packets of energy) and gave the famous Planck Equation  $E = h\nu$ , where  $h$  is the Planck's constant having the value of  $6.626 \times 10^{-34} J$ . In 1905, Einstein adopted Planck's idea of quantization and explained the photoelectric effect which later won him the noble prize. In 1923, Compton with his scattering experiment proved that light was indeed a particle of zero rest mass and energy given by the Planck's equation. This particle was nothing called the photon and was denoted by  $\gamma$ .

Compton found that the light incident on a particle gets shifted in wavelength following the equation

$$\lambda' = \lambda + \lambda_c(1 - \cos\theta)$$

where  $\lambda_c = \frac{h}{mc}$  is the Compton wavelength.[16]

Photons play a very important role in the field of quantum field theory where we take fields to be quantized. Here we picture the interaction between two charges as streams of photons flowing back and forth between them. Thus the classical concept of 'action at a distance' as mediated by fields changes in quantum field theory and here we consider interactions as exchange of particles. Later after many years it was found that photons are the mediators of electromagnetic interaction only and all electromagnetic interactions proceed by the exchange of photons among them. It was also found that like photons there were other mediators like gluons (mediator of strong interaction) and  $Z, W^\pm$  bosons (mediator of weak interaction).

### 1.3 Introduction to the family of Quarks and Leptons

In modern day, all the elementary particles may be grouped under two categories:

- QUARKS
- LEPTONS

**Quarks** are the elementary particles which make the protons and neutrons. They are of 6 different flavours which are subdivided into 3 generations as shown in the table below:

Flavor	Mass(in $\text{Gev}/c^2$ )	Electric Charge in e
<b>u</b> up	0.002	2/3
<b>d</b> down	0.005	-1/3
<b>c</b> charm	1.3	2/3
<b>s</b> strange	0.1	-1/3
<b>t</b> top	173	2/3
<b>b</b> bottom	4.2	-1/3

The quantum number of the above quarks is listed as follows:

Quantum numbers of Quarks							
Particle	Charge	Baryon No.	Spin	Isospin	$I_3$	Charmedness	Strangeness
Up	$2/3e$	$1/3$	$1/2$	$1/2$	$1/2$	0	0
Down	$-1/3e$	$1/3$	$1/2$	$1/2$	$-1/2$	0	0
Charm	$2/3e$	$1/3$	$1/2$	0	0	1	0
Strange	$-1/3e$	$1/3$	$1/2$	0	0	0	-1
Top	$2/3e$	$1/3$	$1/2$	0	0	0	0
Bottom	$-1/3e$	$1/3$	$1/2$	0	0	0	0

Quarks feel all kind of interactions i.e, strong, weak, electromagnetic and gravitational. They readily form bound states and thus cannot be detected directly. The bound states of quarks are called **Hadrons**. Hadrons are categorised into two types:

- **MESONS** ( $q\bar{q}$ )
- **BARYONS** ( $qqq$ )

**Leptons** consists of electrons and neutrinos and they are also divided into 6 flavors and grouped in 3 generations as shown in the table below:

Flavor	Mass(in $\text{Gev}/c^2$ )	Electric Charge in e
e electron	0.000511	-1
$\nu_e$ electron neutrino	0	0
$\mu$ muon	0.106	-1
$\nu_\mu$ muon neutrino	0	0
$\tau$ tau	1.777	-1
$\nu_{\tau}$ tau netrino	0	0

The quantum number of the above leptons is listed as follows:

Quantum numbers of Leptons						
Particle	Charge	Spin	$L_\mu$	$L_e$	$L_\tau$	Isospin
Electron	-1e	$1/2$	0	1	0	0
Muon	-1e	$1/2$	1	0	0	0
Tau	-1e	$1/2$	0	0	1	0
Electron-neutrino	0	$1/2$	0	0	0	0
Muon-neutrino	0	$1/2$	0	0	0	0
Tau-neutrino	0	$1/2$	0	0	0	0

Leptons undergo only weak and gravitational interactions. Charged leptons undergo electromagnetic interaction sometimes. Leptons do not form any bound state with themselves alone and thus we can detect them directly.

## 1.4 Introduction to $D^{*0}$

We saw that quarks form bound states of mesons and baryons. Mesons are made up of a pair of a quark and an anti-quark. So considering the spin addition, mesons may be further classified into:

- Pseudoscalar Mesons
- Vector Mesons

Quarks are fermions and thus are spin half particles. By convention the parity of quarks are taken to be +1 and those of anti-quarks as -1. Thus for a  $q\bar{q}$  bound state, the possible values of spin(J) are 1 and 0 and the parity(P) would always be -1. Mesons with  $J^P=0^-$  are called Pseudoscalar mesons and those with  $J^P=1^-$  are called Vector mesons.

$D^{*0}$  is a vector meson with quark content  $c\bar{u}$ . Thus we can construct the following table for  $D^{*0}$  for its quantum numbers:

Quantum numbers of $D^{*0}$					
Quark Content	Charge	Isopin	$J^P$	charmedness	strangeness
$c\bar{s}$	0	$\frac{1}{2}$	$1^-$	1	0

Till now the measured mass of  $D^{*0}$  is  $2.007 \pm 0.05 GeV/c^2$ . [10]. The measured width of this is still an ambiguity and thus we have a upper limit only which is given by  $< 2.1 MeV$  CL = 90%.

$D^{*0}$  decays through 2 different processes:

- $D^{*0} \rightarrow D^0 \gamma$
- $D^{*0} \rightarrow D^0 \pi^0$

Among them the first decay channel is a radiative channel and is the channel of interest here. In this decay the isospin, charmedness and strangeness all are preserved. The Branching Ratio of this decay is 0.35. This is due to the fact that the other decay channel unlike that of  $D_s^{*+}$  do not violate isospin. Hence the branching ration of the second channel of  $D^{*0}$  is higher as it preserves all the quantum numbers and also is not a radiative decay mode. The decay width of  $D^{*0}$  gets saturated by the two given channels

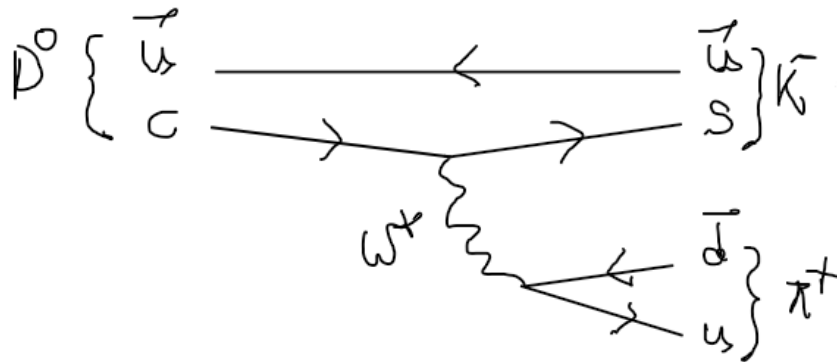


Figure 1.1: Feynmann tree diagram for decay of  $D^0$  meson.

of  $\pi$  and  $\gamma$  and thus  $D^{*0}$  do not decay into any other channel and we get only these two channels in contrast to that of  $D_s^{*+}$  which has a third channel though with much less branching fraction.[1]

$D^{*0}$  on decaying to  $D^0$  and  $\gamma$  or  $\pi$  goes from its excited state to its ground state  $D$  meson,  $D^0$ . However, the meson  $D^0$  is not stable and further decays into a Kaon( $K^-$ ) and a pion( $\pi^+$ ). The feynmann diagram for which is given in Figure-1.1.

# Chapter 2

## Historical Background

Precise measurements of the branching fractions of decays of charmed mesons provide important information about the decay dynamics of these particles. The charm quark is not heavy enough for reliable application of the factorisation approach and heavy quark-expansion tools which are successfully used in B-meson decays. It is also not light enough for the application of chiral perturbation theory which are used in the cases of Kaon decays.[14]

### 2.1 Motivation and Theory

The goal of this analysis is to measure the branching fraction of radiative decay ( $D^{*0} \rightarrow D^0\gamma$ ). The vector mesons  $D^{*0}$  decays via electromagnetic transitions to  $D^0$  and  $\gamma$ . This decay is proportional to the magnetic moment of the constituent quarks [11], which allows an important test of the Standard model for the heavy quark  $c$ . Measurements of lifetimes and branching fractions are an essential test of non-perturbative QCD and can give some guidance as to what is needed to theoretically describe strong interactions at all energy scales [5]. The charmed meson, described as a hydrogen-like hadronic system consisting of a heavy quark ( $c$  quark) and a light quark ( $u$ ,  $d$ , or  $s$  quark), is a particularly suited laboratory to test the effective models mentioned above. The decay branching fractions of  $D^{*0}$  to  $D^0\gamma$  (radiative decay) have been studied by a number of authors based on different effective models [?]. A precise measurement of the branching fractions will constrain the model parameters and thereby help to improve the models used for studying the decay channel. On the experimental side, the branching fractions are critical input values for many measurements such as the open charm cross section in  $e^+e^-$  annihilation [7] and the semileptonic decays of  $B^\pm$  [6].

The branching fractions were previously measured in many electron-positron collision experiments, such as CLEO [8], ARGUS [9], BABAR [1] etc., but the uncertainties

of the averaged branching fractions by the Particle Data Group (PDG) [10] are large (about 8%). The data sample used in this analysis was of luminosity  $482 \text{ pb}^{-1}$  collected at a center-of-mass (CM) energy  $E_{com} = 4.009 \text{ GeV}$  with the BESIII detector. For this analysis, an efficient detection of photons as well as a precise measurement of photon energies is crucial. The photon energy plays a very important role in the reconstruction of the decay  $D^{*0} \rightarrow D^0 \gamma$  because we reconstruct the  $D^{*0}$  directly from  $D^0$  and  $\gamma$ . Unlike the other channel, where the photons combine to form  $\pi^0$ . Here the photon itself combines with  $D^0$  directly and give us the parent particle. The mass difference between the parent and its daughter is also not much and thus because of this small mass difference it is further more important to calculate the photon energy very efficiently with least possibility of error. The mass difference between  $D^{*0}$  and  $D^0$  is,

$$m_{D^{*0}} - m_{D^0} = 142.0 \text{ MeV}/c^2 [10]$$

With its efficient electromagnetic calorimeter (ECL Clusters, described in detail in later section), BELLE II detector is well efficient to get a wide range of photon energies and thus is good suited for this task.

BELLE II also being a new detector has far better statistics than its predecessor, the CLEO and BABAR experiment. Here we get a luminosity of  $100 \text{ fb}^{-1}$  which gives far more number of MC events for the reconstruction of  $D^{*0}$ . This large number of data ensures better results and much better statistical error than what we got from previous analysis. Thus we can measure ther signal yield and thus the branching ratio with much greater accuracy. Also as BELLE II is a B-factory it is specifically designed for the measurement of branching ratios of B-mesons and D-mesons(which are nothing but the daughter of B-mesons). And as it is an ongoing project it is currently taking data every second and thus providing us with more accurate and more number of data as time goes by. The large data may also help us to measure the partial width of  $D^{*0}$  accurately and give an exact value, which till now is quoted only as an upper limit with a confidence level of 90%.

# Chapter 3

## The Belle II Experiment

The Belle II experiment is like the successor of BABAR and Belle, all of which are B factory experiments. The peak luminosity of Belle II is  $8 \times 10^{35} \text{ cm}^{-2} \text{ s}^{-1}$  which is more than 30 times the combined integrated luminosity of both BABAR and Belle. The detector is situated in the interaction region of SuperKEKB  $e^+e^-$  collider at KEK laboratory Tsukuba, Japan. The first collision of asymmetric  $e^+$  and  $e^-$  beams of energies 7 and 4 GeV respectively were recorded in 2018 and from then on the data is constantly been collected.

### 3.1 SuperKEKB and Belle II Detector

The Belle II detector is depicted in Figure-3.1. The interaction point(IP) is surrounded by beryllium beam pipe of low mass, whose diameter is of 2 cm. The small diameter helps to fit two layers of DEPFET silicon pixel detectors(SVD and PXD respectively) in the close proximity of the interaction point. This enables us to detect the decay vertex more accurately and thus helps in the reconstruction of the decay.

Because of the asymmetric nature of the detector, we do not get equal amounts of energy in the forward and backward direction. Forward direction gives the high energy electrons while low energy positron beams are detected in the backward direction. The detector is subdivided into a number of subdetectors as shown in Figure-3.2.

**Beam Pipe** is not an active part of the detector. It separates the detector from the interaction region and minimizes the energy loss. To minimize the energy loss, the beam pipe is constructed to be very thin.[13]

**PXD** stands for Pixel Detector. It measures the position of each particle that goes through this detector with high precision. This helps to determine the intersection point

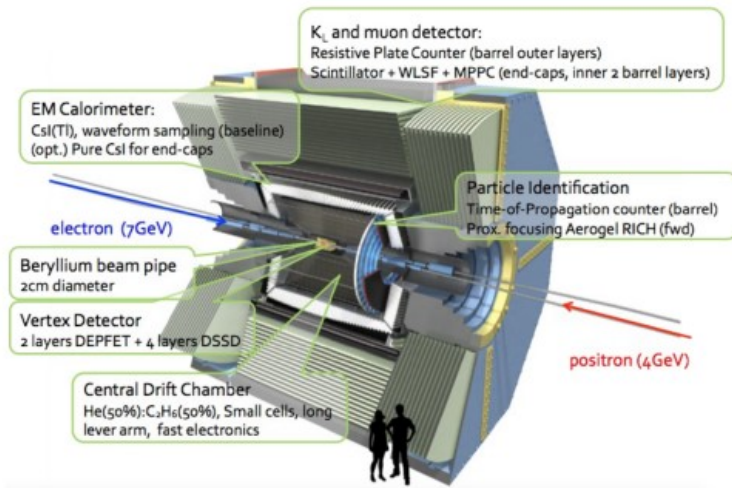


Figure 3.1: Belle II Detector.[12]

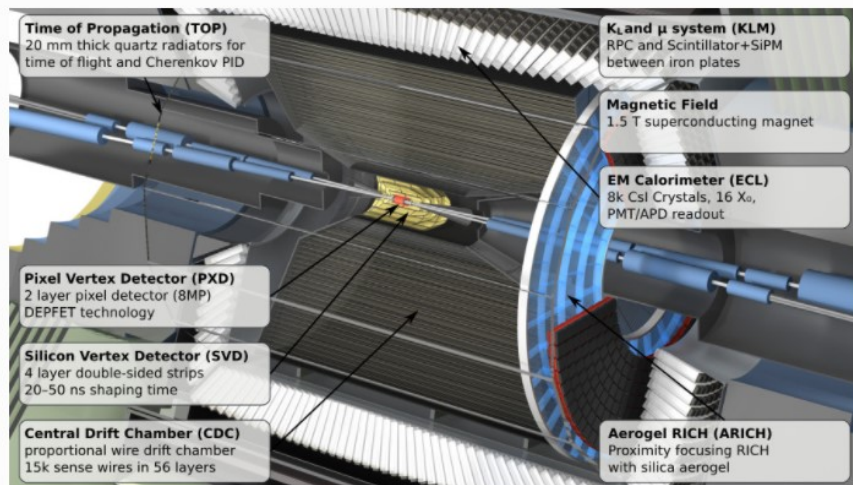


Figure 3.2: Close-up of Belle II Detector indicating all the different sub-detectors.[12]

of different particles. The intersection point(IP),also known as the vertex, represents the point from where all the particles originate or collide.[13]

**SVD** stands for Silicon Vertex Detector and is present at the outer part of the vertex detector. It is made of double sided silicon microstrip sensors that has a width of  $50\ \mu\text{m}$ . [13]

**VXD** is the Vertex Detector. It is nothing but the combination of the SVD and PXD. [13]

**CDC** stands for Central Drift Chamber and is made of sense wires suspended in  $\text{He-C}_2\text{H}_6$  gas. It is the main tracking chamber of Belle II. When a charged particle passes through this gas, it ionises the gas and thus ionisation charges are formed which drift to the sense wires located nearby and causes signal propagation. This is called a "hit" in the CDC. [13]

**TOP** is the Time of Propagation detector. It gives information about particle identification. It works on the principle of Cherenkov effect as the particles passing through it emits Cherenkov photons at an angle that depends on the velocity of the particle. Putting together the information of this velocity along with the measured momentum, from the previous tracking detectors, we get the measurement of the mass and thus the particle can be identified. [13]

**ECL** is the Electromagnetic Calorimeter of Belle II. It measures the electromagnetic energy of photons and electrons and helps in distinguishing electrons from muons. [13]

The tracking detectors also provide particle identification(PID) capability by the process of ionisation energy deposition( $dE/dx$ ) and by measuring the momentum of the charged particles. A axial magnetic field of 1.5 T helps in this process. This magnetic field is generated by a large-bore solenoid which is placed outside the electromagnetic calorimeter(ECL). [13]

## 3.2 The Physics program of Belle II

The previous B factory experiments, Belle and BABAR, operated for a long period of ten years approximately. Their prime objective was to confirm the Kobayashi-Maskawa mechanism for CP violation within the Standard Model(SM). Belle II experiment on the other hand aims to look for deviations from Standard Model and look for new physics beyond the Standard Model. This requires a much larger degree of precision and accuracy which in turn means a very large number of data.

Observation of new physics requires measurements to deviate significantly from the Standard Model predictions. This can happen in two ways:

1. Precise measurement of flavor observables like branching fractions can be shown to deviate from theoretical predictions
2. Rare or forbidden processes can be observed which Standard Model fails to predict.

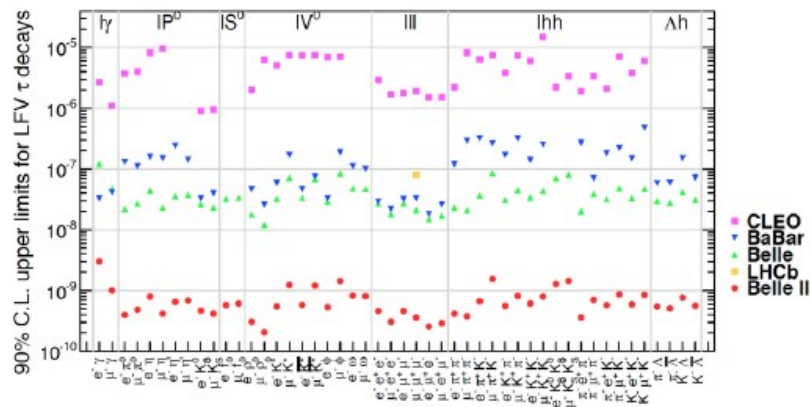


Figure 3.3: Belle II sensitivity to lepton flavor violating decay modes.[5]

Decays that are completely forbidden or extremely rare, as per the predictions of Standard Model, provides definite evidence of new physics being observed. The high cross section for  $c\bar{c}$  indicates that almost 50 billion events of it will be recorded over the whole life of the experiment. This gives very good and powerful resource for the discovery of new physics with very high sensitivity as shown in Figure-3.3.

# Chapter 4

## Software Tools for Analysis

For working with the Belle II detector and analysing the data we need different software tools and frameworks that helps us to access the Belle II data and use it for the reconstruction of different decays. After reocnstructing a particular decay completely, it is analysed and our variables of interest are plotted and fitted with appropriate fitting function. This finally gives us the desired result that we want. Then we are left with comparing the experimental result with the thoeritically calculated ones and comment on the accuracy and precision of the measurement. For rare and forbidden decays, the reconstruction and analysis is done a number of times to make sure we do observe new physics that is beyond the scope of Standard Model.

### 4.1 ROOT

The data to be analysed in high-energy physics experiment is very large and an usable tool is needed for storing and handling such large data. ROOT is an object-oriented framework that has been developed to solve and analyse the data of high-energy physics. It is extremely flexible and provides a programming interface along with a graphical interface for interactive data analysis.

ROOT was developed by CERN and is open sourced so that all high-energy physicists could use it to analyse their data or perform simulations. Not only does it work in C++ but also accepts codes written in Python, showing its great nature of adaptibility which makes it so popular to use in experimental high-energy physics.[15]

The thing that makes ROOT unique is the presence of a data container called **tree**. Tree acts as a sliding window to the raw data stored in a file. A particular entry of tree can contain a number of files, each file containing a huge number of data. Thus we can group the latge number of data and access them very easily using the feature of tree.

This also avoids memory allocation problems while object creation. With its substructures branches and leaves, trees act very efficiently to segregate data and makes it easy to handle for the user. Along with tree, ROOT also has a number of pre-defined function which act very handy while fitting the histograms obtained after the analysis. The graphical user interface of ROOT enable users to plot the data readily in histograms or graphs and draw conclusion from them. Thus ROOT provides a very efficient and user-friendly environment for high-energy physicists to plot and analyze the data efficiently and fitting them accurately to get the desired results.

## 4.2 RooFit

RooFit is a library that provides a toolkit for modeling the expected distribution of events in a physics analysis. The models can be used to perform unbinned maximum likelihood fits, produce plots, and generate "toy Monte Carlo" samples for various studies. We can also combine different pdfs and perform an unbinned likelihood fit with the combined pdf. RooFit was originally developed for the BABAR collaboration, a particle physics experiment at the Stanford Linear Accelerator Center. The software was primarily designed as a particle physics data analysis tool, but its general nature and open architecture make it useful for other types of data analysis also.

### 4.2.1 Mathematical Model

The main function of RooFit is to enable the modeling of distributions of 'event data' of different events in particle physics. Each event is a discrete occurrence in time, and has one or more measured observables associated with it. Experiments of this nature result in datasets obeying Poisson, Gaussian or Binomial statistics. Sometimes it may also follow some statistics which is not predefined but can be obtained by modifying the above mentioned statistic distributions. The natural modeling language for such distributions are probability density functions(p.d.f.s)  $F(x; p)$  that describe the probability density of the distribution of observables  $x$  in terms of a function of parameter  $p$ .

The defining properties of probability density functions, unit normalization with respect to all observables and positive definiteness, also provide important benefits for the design of a structured modeling language. P.d.f.s are easily added with intuitive interpretation of fraction coefficients, they allow construction of higher dimensional p.d.f.s out of lower dimensional building block with an intuitive language to introduce and describe correlations between observables, they also allow the universal implementation of toy Monte Carlo sampling techniques, and are of course an prerequisite for the use of unbinned maximum likelihood fit which is used for the estimation of varous fit parameter.[17]

## 4.2.2 Design

RooFit can be used in both C++ or python language thus showing its versatility. Here each math symbol is presented by a separate object instead of a single entity. A feature of this design philosophy is that all RooFit models always consist of multiple objects. For example a Gaussian probability density function consists typically of four objects, three objects representing the observable, the mean and the sigma parameters, and one object representing a Gaussian probability density function. Similarly, model building operations such as addition, multiplication, integration are represented by separate operator objects and make the modeling language easier to use and also arbitrary models can be modelled easily without complexity.

## 4.3 Basf2

Basf2 stands for **Belle Analysis Software Framework 2**. It consists of a total of 41 packages that meets all the software requirements needed for the experiment. It aids in the interpretation of signals from the detector and gives high-level validation of the performance. The framework is constructed using C++ with an user interface of Python. The major work of Basf2 is to generate simulated data and then reconstructing the preferred decay channel using those data.[13]

The main components of basf2 may be divided into four parts:

- basf2 module
- path
- package
- steering script

### 4.3.1 Modules and Path

In basf2 all the work is done using modules. The modules are arranged in a linear order according to the path given by the user. During data processing, the framework executes the modules of the given path which are executed one after the other in which they are placed in the path.

#### Package

A logical collection of code in basf2 constitute a package. A package consists of many modules and some scripts written in python which configures the path to do some com-

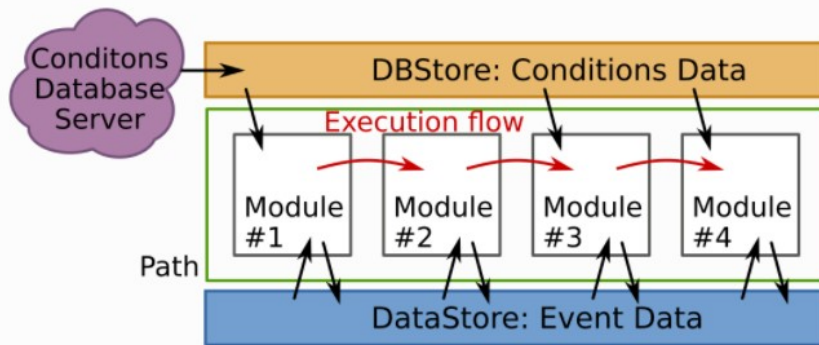


Figure 4.1: Schematic view of flow of process in Basf2.[6]

mon functions. The packages are named after the work that they do or are named after the subdetector that they are related to.

### 4.3.2 Steering Script

The reconstruction code written in python is regarded as the steering script or steering file. A typical script declares a path given by the user as *basf2.path*, configures the modules arranged in that path and then calling *basf2.process* it processes the code and runs, generating certain outputs which are stored in a tree file.

Basf2 has a special analysis package containing python functions which helps us to perform analysis on reconstructed data-objects. These reconstructed data-objects are termed as mdst data-objects. Some of the important mdst data-objects are:

- Track
- ECLCluster
- PIDLikelihood
- MCParticle

The analysis package considers these mdst data-objects as particle candidates. The package operates on the ParticleList which is the list of all the particle candidates in each event and reconstructs them according to the user-defined path, giving us the reconstructed particle that we need.

# Chapter 5

## Analysis of the decay channel of $D^{*0}$

The decay channel of  $D^{*0}$  which we are interested to study is :

$$D^{*0} \rightarrow D^0\gamma, D^0 \rightarrow K^-\pi^+$$

After collecting the data from the detectors, it is simulated to produce MC samples(either generic or signal). From these we get events which contain the raw detector responses. Our prime objective here is to:

- select only those events that are specific to our channel(the **signal**) over those events which are similar in nature but not what we want to study(the **background**).
- calculate the efficiency of our signal selection
- find the total number of events and measure quantities like invariant mass of invariant mass difference between the parent and the daughter particle.

The easiest way of selecting a signal is to apply "cuts" which is nothing but selection over a specific quantity that separates signal from background. Cuts can be applied in sequence to reduce the background even further. Now these events are analysed to reconstruct the particles with high precision, from the daughter particles to the mother particles to get back  $D^{*0}$ , and measure the four-momenta of the particles produced in the interaction.

### 5.1 Reconstruction

The first step of reconstruction is to combine the responses from each sub-detector. This process is called clustering. After combining all the data we look for the channel of our

interest. Before the identification of particles and tracking the particle trajectories we apply some loose selection cuts on the simulated MC data so as to exclude unnecessary backgrounds that are way far from affecting our desired result.

Objects	Pre-Selection Cuts
Tracks	$ dr  < 0.5 \text{ cm}$ and $ dz  < 2 \text{ cm}$
$K^-$	KaonID $\frac{\mathcal{L}_K}{\mathcal{L}_K + \mathcal{L}_\pi} > 0.3$
$\pi^+$	PionID $\frac{\mathcal{L}_\pi}{\mathcal{L}_K + \mathcal{L}_\pi} > 0.3$
$D^0$	$1.8148 < M(K^- \pi^+) < 1.9148 \text{ GeV}/c^2$
$\gamma$	$E_\gamma^{barrel} > 30 \text{ MeV}$ $E_\gamma^{forward} > 120 \text{ MeV}$ $E_\gamma^{backward} > 80 \text{ MeV}$
$D^{*0}$	$1.954 < M(D^0 \gamma) < 2.055 \text{ GeV}/c^2$ $0.058 < \Delta M < 0.194 \text{ GeV}/c^2$

### 5.1.1 Tracking

The first job of reconstruction is tracking. Here we find out the trajectories of the particles using the tracking detectors. At first we find the patterns in the hits in the tracking detector, then we figure out the best possible value of the kinematic variable that describe the particle trajectories corresponding to each hit. This ensures that the particle's position and momentum is close to the interaction region. For our channel we take the variables:

- **dr** representing the transverse distance of the track from the interacting point.
- **dz** point of closest approach in the axial direction, from the interaction point.

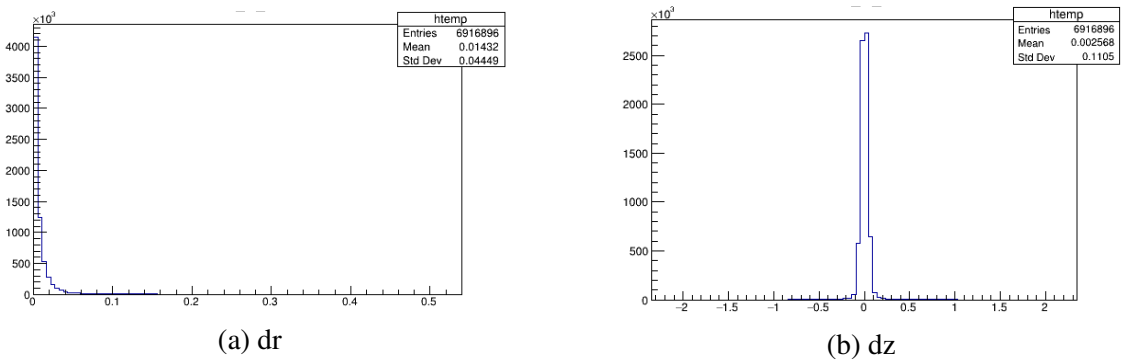


Figure 5.1: dr and dz with their selection cuts

The selection cuts on  $\mathbf{dr}$  for our channel is  $|\mathbf{dr}| < 0.5$  cm (figure-5.1a) and for  $\mathbf{dz}$  is  $|\mathbf{dz}| < 2$  cm (figure-5.1b). The distribution of which are shown in Figure-5.1. We apply these cuts because the particles specific to our channel lies in between this region. Above this the probability of getting our particles is very less(almost equal to zero) so we do not include them in our code. Taking further beyond this region might also add unnecessary background which might affect the proper reconstruction of our desired channel.

## 5.1.2 Particle Identification

On getting the right tracks, we determine the likelihoods of the tracks of different particles. For this channel we need to identify the particles Kaons( $K^\pm$ ) and Pions( $\pi^\pm$ ). Both of whose likelihood can be selected using the likelihood cut  $> 0.3$ . Thus,

- KaonID  $\frac{\mathcal{L}_K}{\mathcal{L}_K + \mathcal{L}_\pi} > 0.3$
- PionID  $\frac{\mathcal{L}_\pi}{\mathcal{L}_K + \mathcal{L}_\pi} > 0.3$

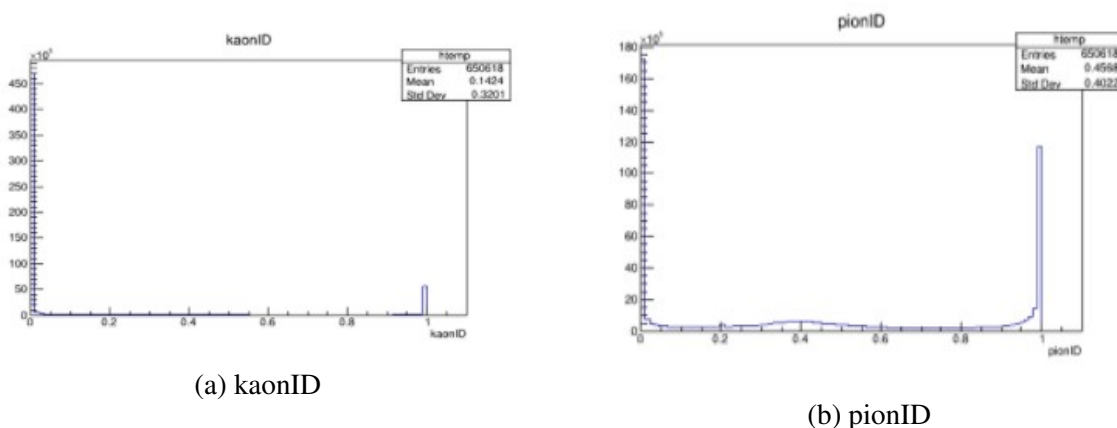


Figure 5.2: kaonID and pionID without any selection cuts

Figure-5.2 shows the Kaon and Pion ID without any selection cuts. We notice that these are mostly located close to 0 or close to 1. After applying the selection cuts we see that for both the pions and kaons the maximum probability of it being present is now close to 1. This is because we have chosen only those kaons and pions that lie in the region  $> 0.3$ . Figure-5.3 shows us the nature of the kaon and pion IDs after the application of the selection cuts.

The gamma is not taken from charged track detectors as it is neutral particle. We take the gamma from the ECL cluster. The cluster region is divided into 3 parts:

- 1 for forward region

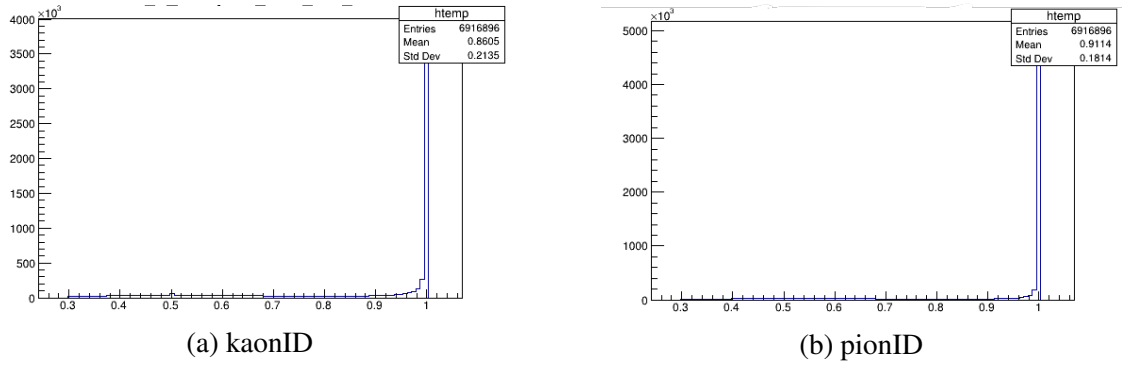


Figure 5.3: kaonID and pionID with their selection cuts

- 2 for barrel region
- 3 for backward region

In the forward region we expect the gamma energy to be  $> 120$  MeV, in the barrel we collect the gammas that have energy  $> 30$  MeV and from the backward region we select those gammas whose energy is  $> 80$  MeV. Thus we can list the selection cuts on gamma as follows:

- for clusterReg==1  $E > 120$  MeV
- for clusterReg==2  $E > 30$  MeV
- for clusterReg==3  $E > 80$  MeV

### 5.1.3 Particle Reconstruction and Variable Declaration

After identifying all the daughter particles produced in the  $e^-e^+$  collision that are of our use, we define a path that reconstructs the parent particle from these daughter particles. Obviously in the identification procedure we have applied cuts on the particles for their precise detection. Appropriate selection cuts are also applied in the reconstruction of the decay path so that we confirm that the particle that we are reconstructing is coming from the channel that we intend to study and not any other channel.

The daughter particles for our decay channel are  $K^-$ ,  $\pi^+$  and  $\gamma$ . After applying the above selection cuts, we reconstruct  $D^0$  from  $K^-$  and  $\pi^+$ . After the reconstruction of  $D^0$  we finally reconstruct our particle of interest,  $D^{*0}$ , according to the following decay channel:

$$D^{*0} \rightarrow D^0 \gamma$$

While reconstruction of  $D^0$  and  $D^{*0}$  we apply some selection cuts to ensure that the particle reconstructed is the particle that we desire for. The selection cuts on  $D^0$  and  $D^{*0}$  are given as follows:

- For  $D^0$  we take a range in which the mass of  $D^0$  lies. The measured mass of  $D^0$  is [10]

$$M_{D^0} = 1.8648 \pm 0.05 \text{ GeV}/c^2$$

So we take the range  $1.8148 < M(K^- \pi^+) < 1.9148 \text{ GeV}/c^2$  as a selection cut for reconstruction of  $D^0$ .

- Similarly for  $D^{*0}$  we take a range in which the mass of  $D^*$  lies. The measured mass of  $D^*$  is [10]

$$M_{D^{*0}} = 2.007 \pm 0.05 \text{ GeV}/c^2$$

So we take the range  $1.954 < M(D^0 \gamma) < 2.055 \text{ GeV}/c^2$  as a selection cut for reconstruction of  $D^{*0}$ .

- Along with mass selection cuts, we also apply a cut on the mass difference between  $D^0$  and  $D^{*0}$ . Theoretically the mass difference between  $D^{*0}$  and  $D^0$  is given by [10]

$$\Delta M_{D^{*0}-D^0} = 0.142 \pm 0.03 \text{ GeV}/c^2$$

So we take the range  $0.058 < \Delta M < 0.194 \text{ GeV}/c^2$  as a second selection cut for the reconstruction of  $D^{*0}$ .

- We also apply a cut on the momentum in the centre of mass frame for  $D^{*0}$ . We choose that the centre of mass frame momentum  $p_{cm}(D^{*+}) > 2.5 \text{ GeV}/c$ .

Thus we see that we took only one selection cut for  $D^0$  while we took a total of three selection cuts for  $D^{*0}$ . This is done for the sole reason to precisely reconstruct the  $D^{*0}$  particle as it is the parent particle that we want to study.

We then define a set of variables for each particle that we have reconstructed. These variables are the ones whose nature and distribution will tell us the accuracy and precision of the reconstruction and hence will give us our final results that we want. These variable can be energy, invariant mass, four-momentum, etc. Basf2 itself provides us with a lot of pre-defined variables that can be used very easily. Among all the variables the most important one is the MC truth matching variable. The **isSignal** variable acts as a boolean and returns **1** if the particle is correctly reconstructed according to the path provided, else it returns **0**. This helps us to distinguish between the **signal** and the **background**. The MC matching is done only for particles that have been reconstructed to check the accuracy and correctness of the reconstruction.

## 5.2 Observation from Histograms

After the successful reconstruction of  $D^{*0}$  and  $D^0$  we plot the distribution of the variables assigned to them in histograms using the software ROOT. While plotting the histograms we do the MC mathing by using the isSignal boolean to separate out the signal and background. The histograms of the signal gives the mean values of the variables of the corresponding particle. By comparing this mean value with the theoretical value that we know we get the idea that our reconstruction is correctly carried out. This confirms that the particle that we reconstructed is the one that which we are looking for and follows the decay channel that we are studying.

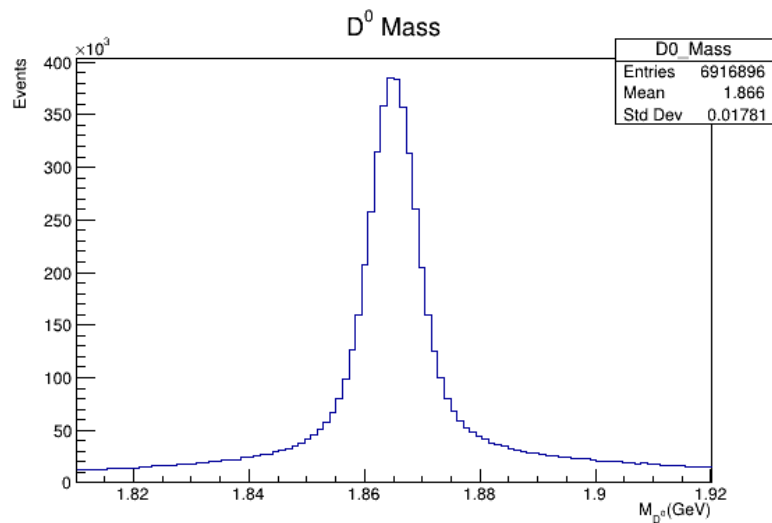


Figure 5.4: Total Mass distribution of  $D^0$ .

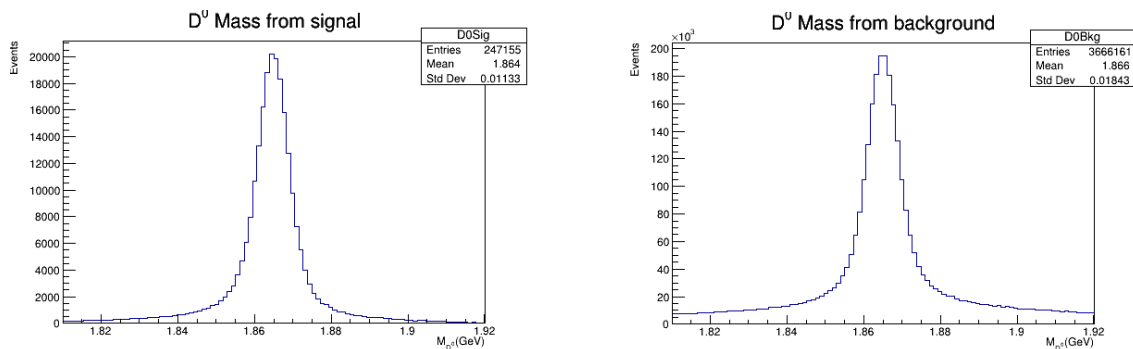
### 5.2.1 Mass of $D^0$

The mass of  $D^0$  is calculated from the kinematic variables of  $K^-$  and  $\pi^+$  by four momenta conservation.

Figure-5.4 shows the mass of  $D^0$  obtained from the masses of  $K^-$  and  $\pi^+$ . We use the four momenta conservation and calculate the mass of  $D^0$  by adding the distribution of masses for  $K^-$  and  $\pi^+$ .

From the Figure-5.4 we can see that we get a sharp peak at the middle and the mean value of the distribution is  $1.866 \text{ GeV}/c^2$  which is very close to the theoretical value of  $D^0$  mass. Now to confirm that the  $D^0$  that we observe in Figure-5.4 is coming from

the channel(path) that we want, we have to do the MC truth-matching. The MC truth-matching is done by the isSignal variable. We give the condition that if the boolean gives 1 then the distribution that we get is considered as the signal (Figure-5.5a) and if it returns 0 the distribution is considered as the background (Figure-5.5b).



(a)  $D^0$  mass distribution from signal

(b)  $D^0$  mass distribution from background

Figure 5.5: Mass distribution of  $D^0$

## 5.2.2 Mass of $D^{*0}$

We calculate the mass distribution for  $D^{*0}$  by taking the four momenta conservation of  $D^0$  and  $\gamma$ . At first we take the total mass distribution of  $D^0$  without doing the MC truth-matching and evaluate the total mass distribution for  $D^{*0}$ . Figure-5.6 does not show clearly any significant peak and thus we have no conclusive evidence that the mass distribution that we see is for  $D^{*0}$ . The reason for the distribution to not have any significant peak is because we took the mass distribution of  $D^0$  from the total range without doing the MC truth-matching.

From the Figure-5.6 we can see two small peaks, one at the beginning around 1.94 and one around 2.00. Though the theoretically predicted mass of  $D^{*0}$  is close to 2 but still the peak is too small to draw any conclusive evidence that the above mass distribution is of  $D^{*0}$ . Thus to have conclusive evidence of the formation of  $D^{*0}$  from  $D^0$  and  $\gamma$ , we perform the MC truth-matching to get signal which provides conclusive evidence of the formation of  $D^{*0}$  as our final reconstructed particle.

From Figure-5.7a we can see that we get a clear peak in the range 1.98 to 2.02. The mean value of the distribution is also given as  $2.002 \text{ GeV}/c^2$  which is very close to the theoretically predicted mass of  $D^{*0}$  ( $M_{D^{*0}} = 2.007 \pm 0.05 \text{ GeV}/c^2$ ) [10].

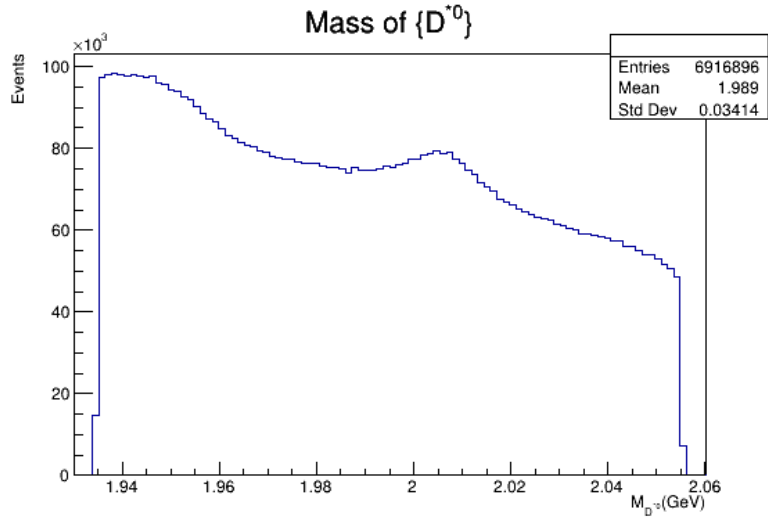
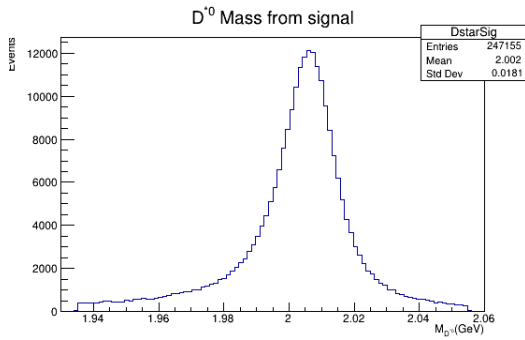
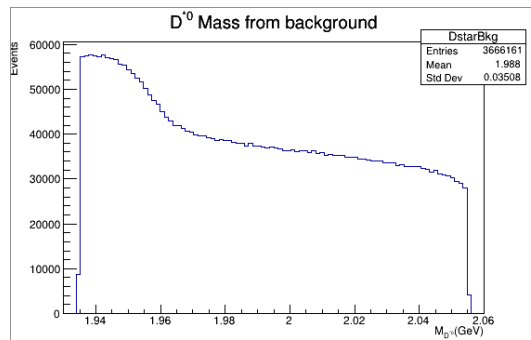


Figure 5.6: Total Mass distribution of  $D^{*0}$ .



(a)  $D^{*0}$  mass distribution from signal



(b)  $D^{*0}$  mass distribution from background

Figure 5.7: Mass distribution of  $D^{*0}$

### 5.2.3 Mass difference between $D^{*0}$ and $D^0$

As we have got the distributions of  $D^{*0}$  mass and  $D^0$  mass, we can easily calculate the distribution for the mass difference between the two. Here we start directly considering the  $D^{*0}$  from the MC truth-matching condition and then calculating the mass distribution of  $\Delta M$  by subtracting the distributions of  $D^{*0}$  mass and  $D^0$  mass. This is because without the MC truth-matching we did not have any conclusive distribution for  $D^{*0}$  mass. We failed to obtain any significant peak of  $D^{*0}$  as was seen in Figure-5.6. So we calculate the mass difference  $\Delta M$  in the MC truth-matching condition of  $D^{*0}$ , where  $\Delta M = M_{D^{*0}} - M_{D^0}$ .

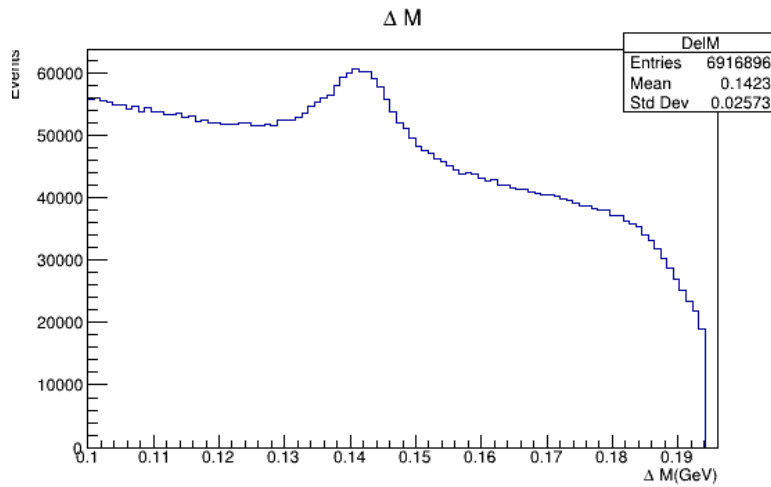
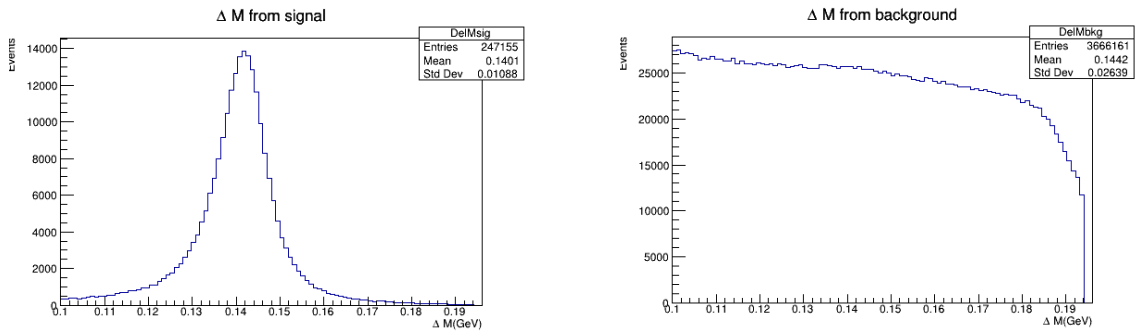


Figure 5.8: Distribution of mass difference of  $D^{*0}$  and  $D^0$ .



(a) Mass difference of  $D^{*0}$  and  $D_s^0$  from signal    (b) Mass difference of  $D^{*0}$  and  $D_s^0$  from background

Figure 5.9: Distribution of Mass difference of  $D^{*0}$  and  $D^0$

Figure-5.8 shows a peak around the range 0.13 to 0.15 and the mean value is given

as  $0.1423 \text{ GeV}/c^2$  which is close to the theoretically predicted mass difference between  $D^{*0}$  and  $D^0$ . Now we apply the `isSignal` boolean to check for the signal and background, so as to confirm how many of our reconstructed particles fall under the channel that we intend to study.

The signal distribution (figure-5.9a) shows a very good and significant peak with the mean value of  $\Delta M$  as  $0.1401 \text{ GeV}/c^2$ , which is very close to the theoretical value. Thus we can conclude that the particles reconstructed in our code are  $D^{*0}$  and  $D^0$  and they have been successfully reconstructed from the decay channel that we are interested in.

# Chapter 6

## Optimization of the reconstructed decay channel of $D^{*0}$

Now we have the mass distributions of  $D^{*0}$  and  $D^0$  which are in good agreement with the theoretical values. The mass difference between these two also matches the theoretically quoted value. These values that we obtained were by applying some loose initial selection cuts. We can further add tight cuts to optimize the result and make it even more accurate.

This is done by the method of "cut and count". Here we calculate the figure of merit(FOM) for certain particle kinematic variables which have high chances of adding error and background to the result obtained. In this technique we try to maximize the selection of signal and the rejection of background. After doing this and applying the cut that we obtain from this technique we confirm that the  $D^{*0}$  and  $D^0$  distributions that we get are purely from the decay channel under study with minimum inclusion or effect from the background.

### 6.1 Cut and Count Method

To know the particle kinematic variables that directly affects the distribution of  $D^{*0}$  and  $D^0$ , we study the overlay plots of all the possible kinematic variables that we have defined during our reconstruction and check which of them shows a sharp difference between the distribution of the signal and the background.

Those kinematic variables where the signal and background overlay distribution lays one over the other or shows very little differences are not considered for optimisation. This is because while applying a tighter cut on such variables reduces the background

very much but due to the similar nature of the signal, it also gets reduced. This is not at all accepted for the analysis as the signal is the one which we study for the confirmation and correctness of the reconstruction. So for accurate and proper result we desire to have as much signal as possible and reduce the background as much as possible. Thus kinematic variable overlays which shows sharp difference between the signal and background distribution are chosen for optimisation. This ensures that applying a cut only reduces the background by much extent and does not effect the signal much.

Here we use the N-1 method of optimisation for the "cut and count" method. In N-1 optimisation, we at first plot the overlay distribution of all the kinematic variables and choose those kinematic variables which showed sharp difference between the distributions of signal and background. Then we take one such kinematic variable and calculate their figure of merit and the appropriate new cut value which would give more signal and lesser background, i.e., the signal selection efficiency is high and background selection efficiency is low. After that we apply the cut in our reconstruction script and get the distribution of  $\Delta M$ , i.e., the mass difference between  $D^{*0}$  and  $D^0$ , for this cut. This distribution of  $\Delta M$  is the result of the first optimisation. After first optimisation we again plot the selected kinematic variables and check their overlay distributions. Some kinematic variables, which showed difference in the overlay plots of signal and background distributions previously, but after applying the cut for first optimisation might not show significant difference between the signal and background. Such kinematic variables are then not considered for optimisation and those kinematic variables which still showed significant difference between the signal and background distribution are considered for the second optimisation.

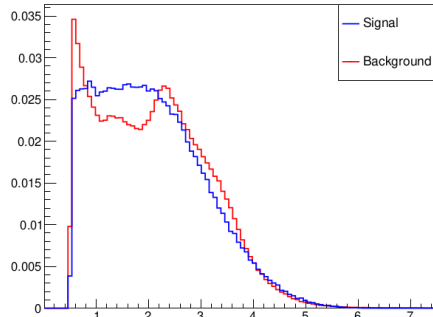
Thus each time we optimise a kinematic variable and apply a tighter cut, we plot all the other kinematic variables to check whether that new cut had any effect on the previously selected kinematic variables. This way we apply cuts and optimise the kinematic variables which are independent of each other and this method of optimisation is called the N-1 optimisation. Also for each optimisation we plot the distribution of  $\Delta M$  by applying suitable cuts so as to confirm the reducing of the background and to get the final  $\Delta M$  which is the distribution that we analyse and fit in the end to get the final result and conclude the proper reconstruction and analysis of the particle and channel that we are studying.

## 6.2 Variable Selection

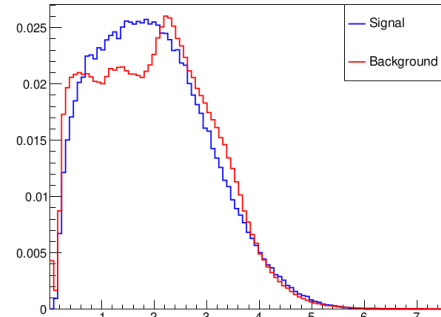
The first step of the cut and count is the selection of the variables which shows significant differences in the distribution of signal and background in its overlay plots. For this we plot the overlay plots for all the kinematic variables of the daughter particles.

## 6.2.1 Kaons( $K^-$ )

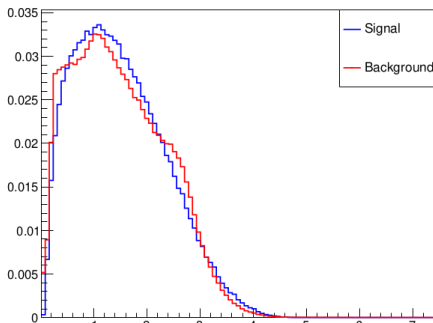
Figure-6.1(a-f) shows the overlay plots of the kinematic variables of Kaon( $K^-$ ). By



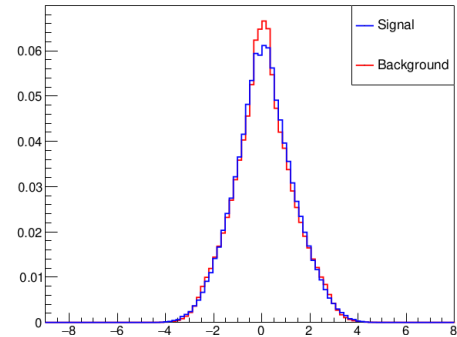
(a) Overlay plot of  $K^-$  energy



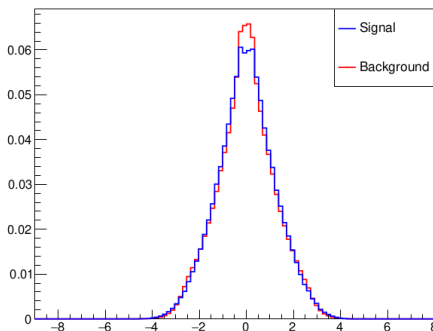
(b) Overlay plot of  $K^-$  momentum



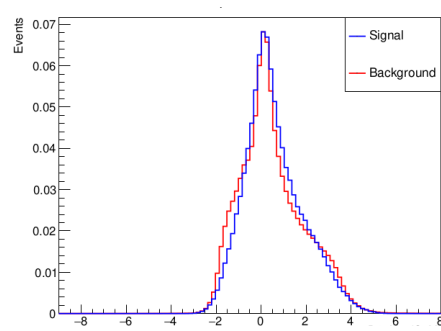
(c) Overlay plot of  $K^-$  transverse momentum



(d) Overlay plot of  $K^-$  momentum in x-direction



(e) Overlay plot of  $K^-$  momentum in y-direction



(f) Overlay plot of  $K^-$  momentum in z direction

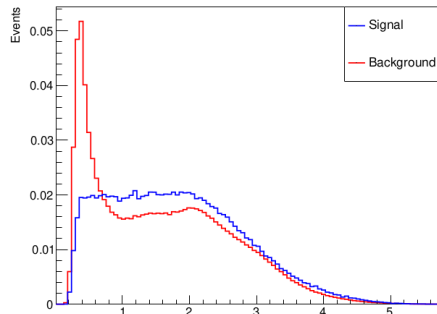
Figure 6.1: Overlay plots of Kaon ( $K^-$ )

looking at the plots of Figure-6.1 we can see that none of the overlay plots of any kinematic variable of  $K^-$  shows distinct difference in the distribution of the signal and the background. The signal and background distributions are almost lying one on top of the other. So applying a cut would not only reduce the background but also reduce the signal by the same amount and that we do not want. **Thus none of the kinematic**

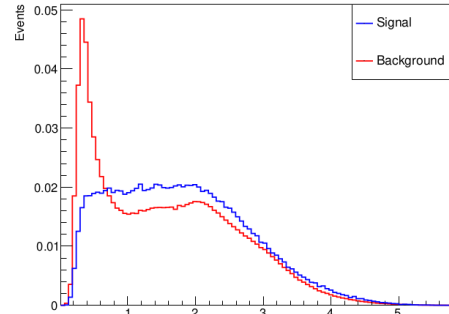
variables of Kaon ( $K^-$ ) are chosen for the optimisation process.

## 6.2.2 Pions( $\pi^+$ )

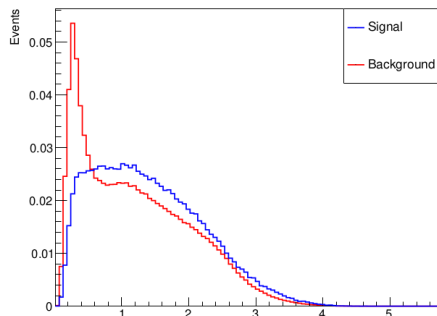
Figure-6.2(a-f) shows the overlay plots of the kinematic variables of Pion( $\pi^+$ ). Here



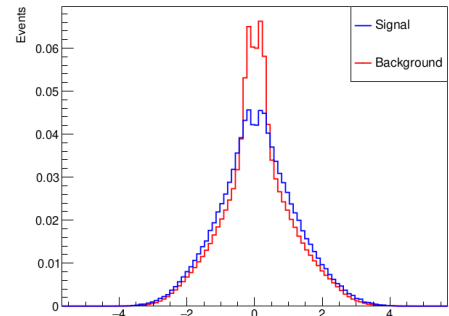
(a) Overlay plot of  $\pi^+$  energy



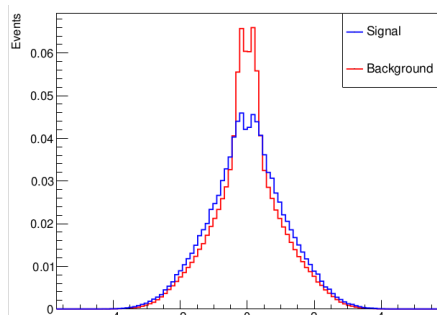
(b) Overlay plot of  $\pi^+$  momentum



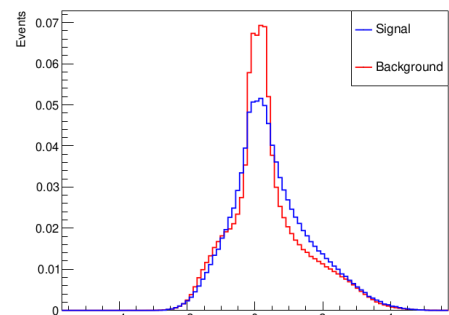
(c) Overlay plot of  $\pi^+$  transverse momentum



(d) Overlay plot of  $\pi^+$  momentum in x-direction



(e) Overlay plot of  $\pi^+$  momentum in y-direction



(f) Overlay plot of  $\pi^+$  momentum in z direction

Figure 6.2: Overlay plots of Pion ( $\pi^+$ )

also we see that from the plots of Figure-6.2 we cannot find any overlay plots of any kinematic variable of  $\pi^+$  which shows distinct difference in the distribution of the signal and the background. The signal and background distributions are almost lying one on

top of the other. So applying a cut would not only reduce the background but also reduce the signal by the same amount and that we do not want. **Thus none of the kinematic variables of Pion ( $\pi^+$ ) are chosen for the optimisation process.**

### 6.2.3 $\gamma(\gamma)$

Figure-6.3(a-f) shows the overlay plots of the kinematic variables of gamma( $\gamma$ ).

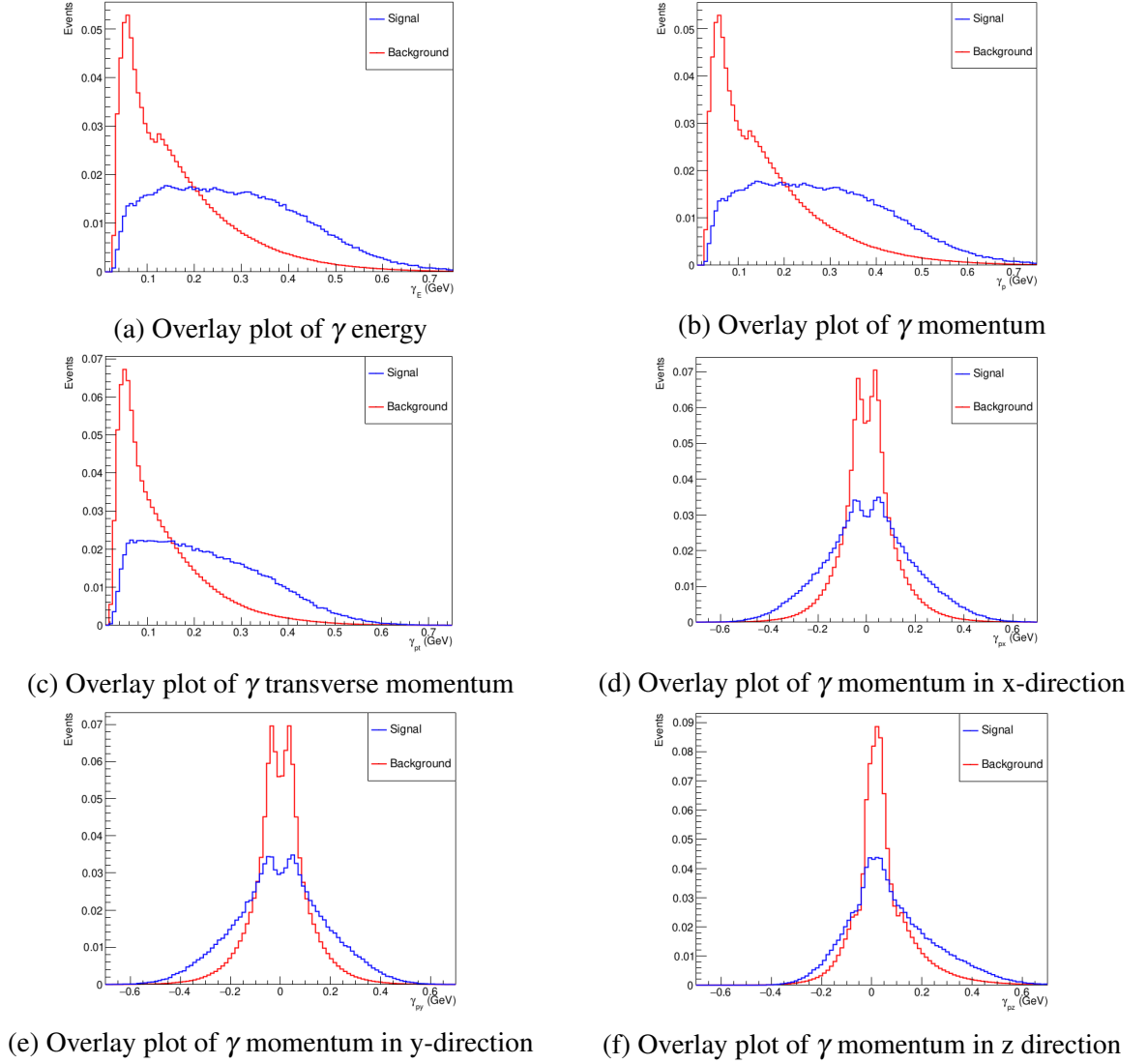


Figure 6.3: Overlay plots of gamma ( $\gamma$ )

Here we see from Figure-6.3a, Figure-6.3b and Figure-6.3c that the signal and background shows significant difference in their distributions. They are not lying totally on

top of each other. Thus applying a proper cut will reduce the background very much without affecting the signal. Thus we choose the  $\gamma$  energy and  $\gamma$  transverse momentum as the kinematic variables of gamma for the optimisation process. On looking at Figure-6.3a and Figure-6.3b will show that both have similar overlay plots and thus only one among them is chosen and so we choose Figure-6.3a. The other kinematic variables of gamma do not show much significant difference between signal and the background and hence are not chosen for the optimisation process.

Now as mentioned before that the gamma particle comes from three regions: forward, backward and barrel, referred as the cluster regions(clusterReg) in basf2. We have seen that

- clusterReg==1 is for forward region
- clusterReg==2 is for barrel region
- clusterReg==3 is for backward region

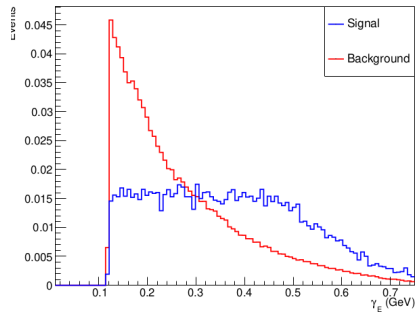
So we also plot the kinematic variables of gamma in all the three regions and see whether any kinematic variable is obtained that can be used for the optimisation process.

## 6.2.4 $\gamma$ in forward region(clusterReg==1)

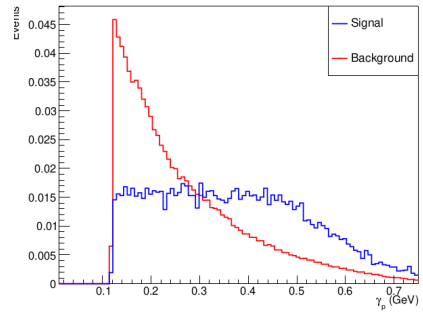
Figure-6.4(a-f) shows the overlay plots of the kinematic variables of gamma( $\gamma$ ) in the forward region(clusterReg==1).

We can see that in the forward region some gamma kinematic variables show good distinction between the signal and background distribution. Thus Figure-6.4a, Figure-6.4b, Figure-6.4f and Figure-6.4c can be chosen for the optimisation process. Again due to the similar nature of Figure-6.4a and Figure-6.4b we only choose one of them and like the previous selection, we choose the gamma energy(in forward region) over the gamma momentum(in forward region). The sole reason to do this is that if we choose the gamma momentum(in forward region) instead of gamma energy(in forward region) then the other chosen variable which is the gamma transverse momentum(in forward region) is not an independent kinematic variable anymore. It thus gets affected once we optimise the gamma momentum(in forward region) and vice versa and thus one of our kinematic variables for optimisation gets reduced and thus significant reducing of background may not happen.

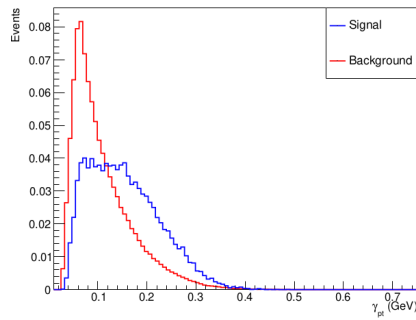
Thus we choose the  $\gamma$  energy(in forward region),  $\gamma$  momentum in z-direction(in forward region) and  $\gamma$  transverse momentum(in forward region) as the kinematic variables



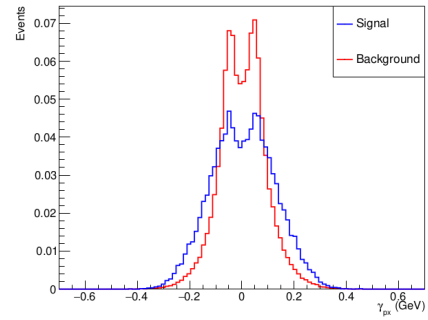
(a) Overlay plot of  $\gamma$  energy



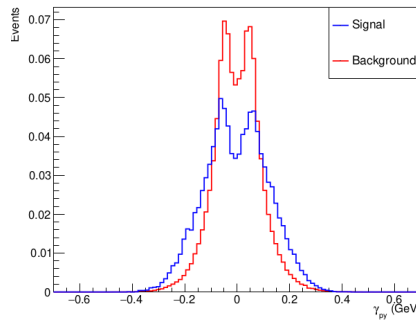
(b) Overlay plot of  $\gamma$  momentum



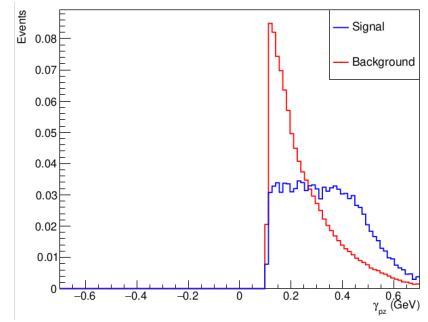
(c) Overlay plot of  $\gamma$  transverse momentum



(d) Overlay plot of  $\gamma$  momentum in x-direction



(e) Overlay plot of  $\gamma$  momentum in y-direction



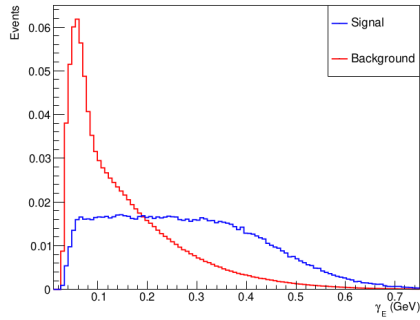
(f) Overlay plot of  $\gamma$  momentum in z direction

Figure 6.4: Overlay plots of gamma ( $\gamma$ ) in the forward region(clusterReg==1)

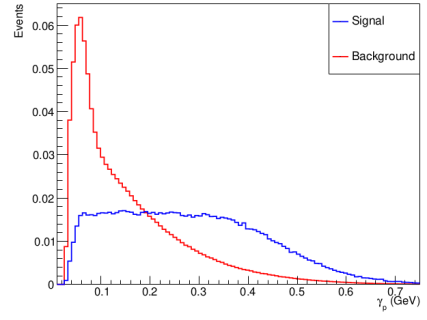
for optimisation from the 1st cluster region( $\text{clusterReg}==1$ ). The other kinematic variables do not show much significant difference between signal and the background and hence are not chosen for the optimisation process.

### 6.2.5 $\gamma(\gamma)$ in barrel region( $\text{clusterReg}==2$ )

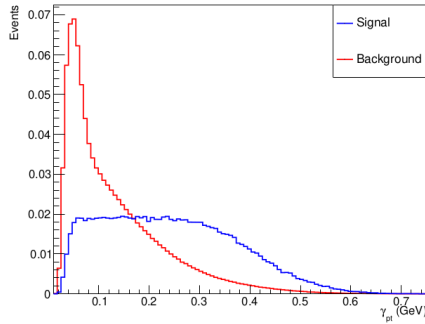
Figure-6.5(a-f) shows the overlay plots of the kinematic variables of  $\gamma(\gamma)$  in the barrel region( $\text{clusterReg}=2$ ).



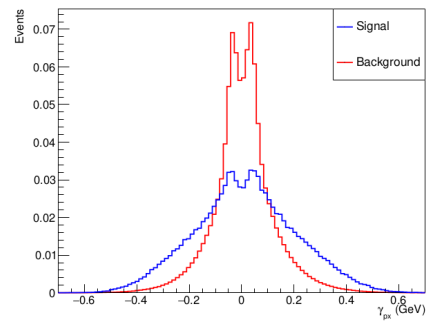
(a) Overlay plot of  $\gamma$  energy



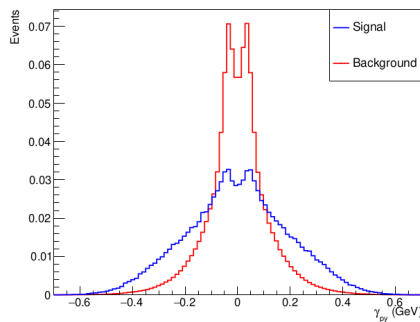
(b) Overlay plot of  $\gamma$  momentum



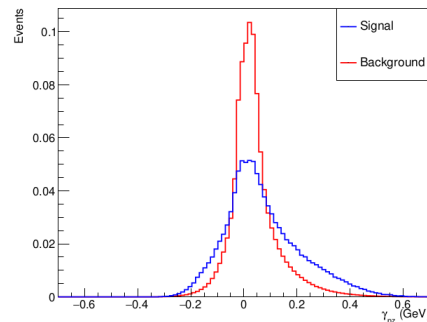
(c) Overlay plot of  $\gamma$  transverse momentum



(d) Overlay plot of  $\gamma$  momentum in x-direction



(e) Overlay plot of  $\gamma$  momentum in y-direction



(f) Overlay plot of  $\gamma$  momentum in z direction

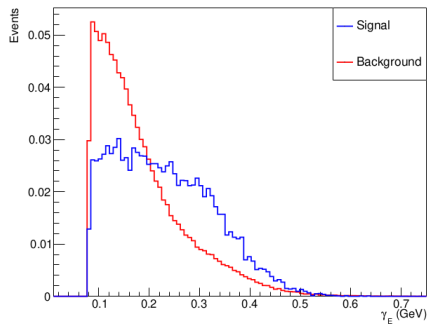
Figure 6.5: Overlay plots of  $\gamma(\gamma)$  in the barrel region( $\text{clusterReg}==2$ )

We can see that in the barrel region also some gamma kinematic variables show good distinction between the signal and background distribution. Thus Figure-6.5a, Figure-6.5b and Figure-6.5c can be chosen for the optimisation process. Again due to the similar nature of Figure-6.5a and Figure-6.5b we only choose one of them and like the previous selection, we choose the gamma energy(in barrel region) over the gamma momentum(in barrel region).

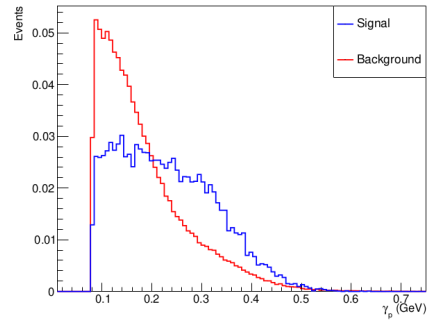
Thus we choose the  $\gamma$  energy(in barrel region) and  $\gamma$  transverse momentum(in barrel region) as the kinematic variables for optimisation from the 2nd cluster region(clusterReg==2). The other kinematic variables do not show much significant difference between signal and the background and hence are not chosen for the optimisation process.

### 6.2.6 $\gamma$ in backward region(clusterReg==3)

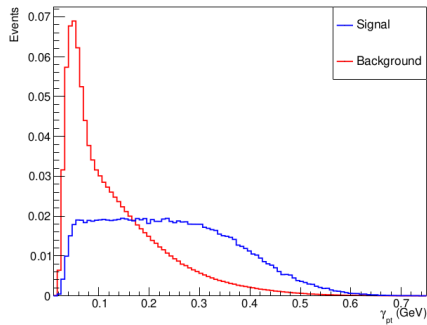
Figure-6.6(a-d) and Figure-6.7(a,b) shows the overlay plots of the kinematic variables of gamma( $\gamma$ ) in the backward region(clusterReg=3).



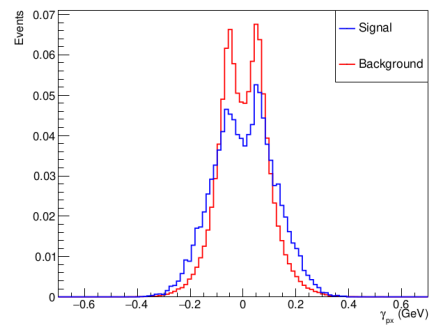
(a) Overlay plot of  $\gamma$  energy



(b) Overlay plot of  $\gamma$  momentum

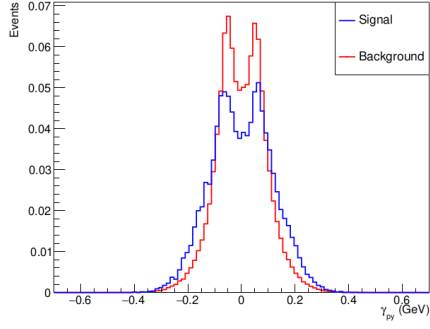


(c) Overlay plot of  $\gamma$  transverse momentum

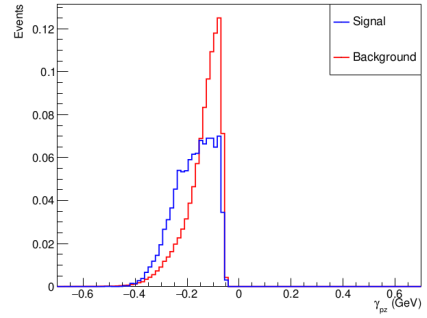


(d) Overlay plot of  $\gamma$  momentum in x-direction

Figure 6.6: Overlay plots of gamma ( $\gamma$ ) in the backward region(clusterReg==3)



(a) Overlay plot of  $\gamma$  momentum in y-direction



(b) Overlay plot of  $\gamma$  momentum in z direction

Figure 6.7: Overlay plots of gamma ( $\gamma$ ) in the backward region(clusterReg==3)

Here also we can see that in the backward region some gamma kinematic variables show good distinction between the signal and background distribution. Thus Figure-6.6a, Figure-6.6b and Figure-6.6c can be chosen for the optimisation process. Again due to the similar nature of Figure-6.6a and Figure-6.6b we only choose one of them and like the previous selection, we choose the gamma energy(in backward region) over the gamma momentum(in backward region).

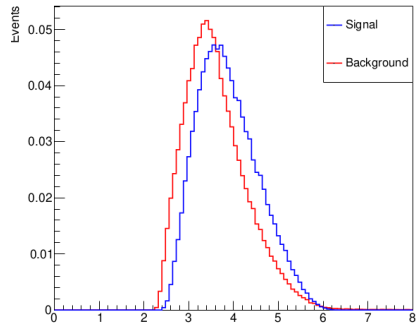
Thus we choose the  $\gamma$  energy(in backward region) and  $\gamma$  transverse momentum(in backward region) as the kinematic variables for optimisation from the 3rd cluster region(clusterReg==3). The other kinematic variables do not show much significant difference between signal and the background and hence are not chosen for the optimisation process.

## 6.2.7 $D^0$ meson

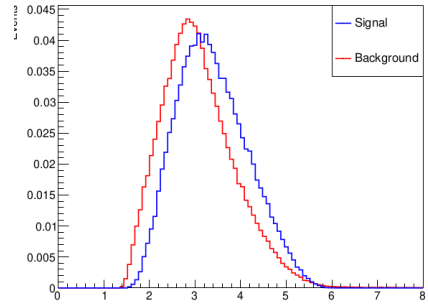
Figure-6.8(a-f) shows the overlay plots of the kinematic variables of  $D^0$ . Here we see that some  $D^0$  kinematic variables show good distinction between the signal and background distribution.

Thus Figure-6.8a, Figure-6.8b and Figure-6.8c can be chosen for the optimisation process. This time however we choose both the  $D^0$  momentum and the  $D^0$  energy as the momentum overlay plot is not exactly similar to the energy plot for  $D^0$ . Thus we choose the  $D^0$  energy,  $D^0$  momentum and  $D^0$  transverse momentum as the kinematic variables for optimisation. The other kinematic variables do not show much significant difference between signal and the background and hence are not chosen for the optimisation process.

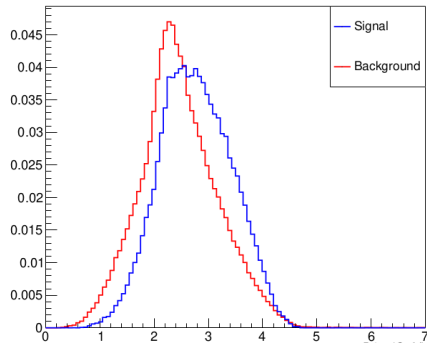
Now looking all the overlay plots that we got for the kinematic variables of the



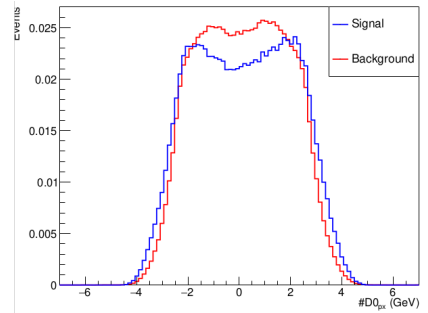
(a) Overlay plot of  $D^0$  energy



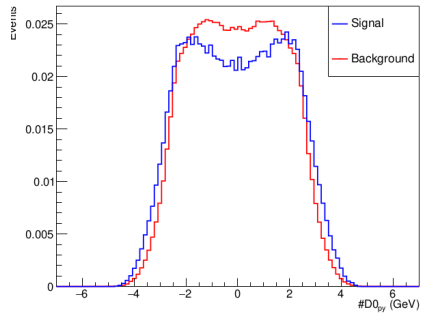
(b) Overlay plot of  $D^0$  momentum



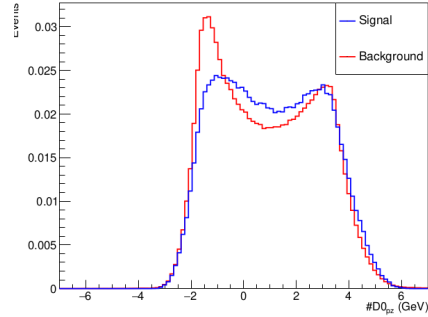
(c) Overlay plot of  $D^0$  transverse momentum



(d) Overlay plot of  $D^0$  momentum in x-direction



(e) Overlay plot of  $D^0$  momentum in y-direction



(f) Overlay plot of  $D^0$  momentum in z direction

Figure 6.8: Overlay plots of  $D^0$

daughter particles we select the variables that look good for optimisation process. The list of such kinematic variables are:

1.  $\gamma$  energy
2.  $\gamma$  transverse momentum
3.  $\gamma$  energy(in clusterReg==1)
4.  $\gamma$  transverse momentum(in clusterReg==1)
5.  $\gamma$  momentum in z-direction(in clusterReg==1)
6.  $\gamma$  energy(in clusterReg==2)
7.  $\gamma$  transverse momentum(in clusterReg==2)
8.  $\gamma$  energy(in clusterReg==3)
9.  $\gamma$  transverse momentum(in clusterReg==3)
10.  $D^0$  energy
11.  $D^0$  momentum
12.  $D^0$  transverse momentum

Then we start the optimisation by optimising each kinematic variable. After optimisation of one variable we put the respective new cut on our reconstructed decay channel and look at the overlay plots of all the other selected kinematic variables to see whether they still showed significant difference between signal and background distribution. Then we do the next optimisation with another variable and continue the optimisation process till all the above selected variables are either optimised or they become unimportant for further optimisation due to some prior optimisation. This is the procedure of N-1 optimisation.

After each optimisation we plot the overlay distribution of the signal and the background for the mass difference between  $D^{*0}$  and  $D^0$ , i.e., the  $\Delta M$ , to check the result of optimisation on our final state particles and for further analysis and calculation. It is the distribution of  $\Delta M$  that we later use for final fitting and for calculating the signal selection efficiency and yield. The mean and errors are also calculated from this distribution and is compared with the theoretical value to confirm the correctness of our reconstructed decay channel and analysis.

### 6.3 First Optimisation

Before optimising any kinematic variable, the overlay plot of  $\Delta M$  looks like as shown in Figure-6.9 We can see that the background is very much more than the signal and

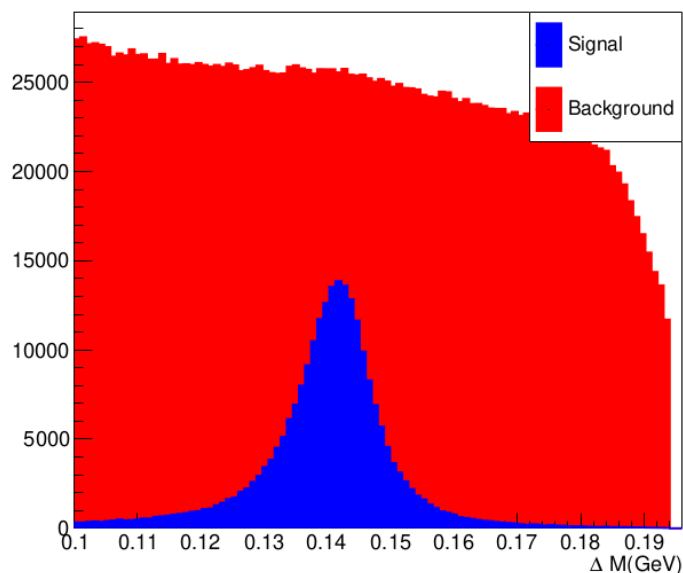


Figure 6.9: Overlay plot of mass difference of  $D^{*0}$  and  $D^0$ .

the signal is just a small peak in the middle(blue region). The height of background is far more than that of signal and hence it needs to be reduced for proper analysis and calculation.

**In the first optimisation we optimise the kinematic variable  $\gamma$  energy.** We find the figure of merit(FOM) plot for this respective kinematic variable and calculated the signal selection efficiency and the background selection efficiency. Then we choose such a value for the  $\gamma$  energy for which we get high signal selection efficiency and low background selection efficiency,i.e., high background rejection efficiency.

In Figure-6.10,  $\epsilon_s$  denotes the signal selection efficiency and  $\epsilon_b$  denotes the background selection efficiency. The background rejection efficiency is calculated by subtracting the background selection efficiency from 1. Looking at the signal selection values and background selection values from Figure-6.10 we see that for  $\gamma$  energy  $\geq 0.13$  GeV we get signal selection efficiency ( $\epsilon_s$ ) = 81% and background rejection efficiency ( $1 - \epsilon_b$ ) = 51%. The value of FOM is also high close to 0.61. Thus after the first optimisation the final selection cut on the energy of  $\gamma$  is  $\gamma_E \geq 0.13$  GeV.

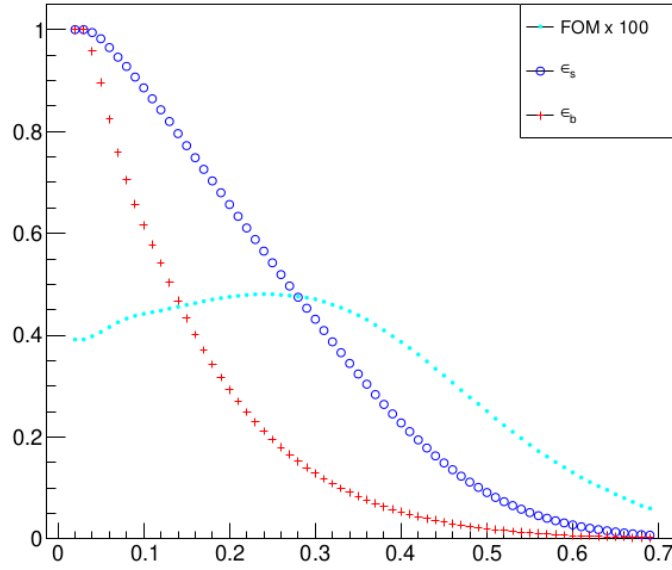


Figure 6.10: Figure of merit plot for  $\gamma$  energy

## 6.4 Second Optimisation

On getting the final selection cut on  $\gamma$  energy we apply that cut and get the overlay distribution of  $\Delta M$ . Figure-6.11 shows the  $\Delta M$  overlay plot after the 1st optimisation. We can see that compared to Figure-6.9, Figure-6.11 shows a much lesser amount of background. The background height has greatly reduced and is now at same height as the signal. Thus we can conclude that the selection cut obtained after the first optimisation had good effect in reducing the background.

Now, total number of signal events before 1st optimisation, i.e., total number of signal events from reconstruction = 247155.

Number of signal events after 1st optimisation = 202858.

The signal efficiency  $\eta$  for the Nth optimisation is defined as,

$$\eta = \frac{\text{Number of signal events after Nth optimisation}}{\text{Total number of signal events before any optimisation}} \times 100\% \quad (6.1)$$

Thus, after 1st optimisation the signal efficiency

$$\eta = \frac{202858}{247155} \times 100\% = 81.97\%$$

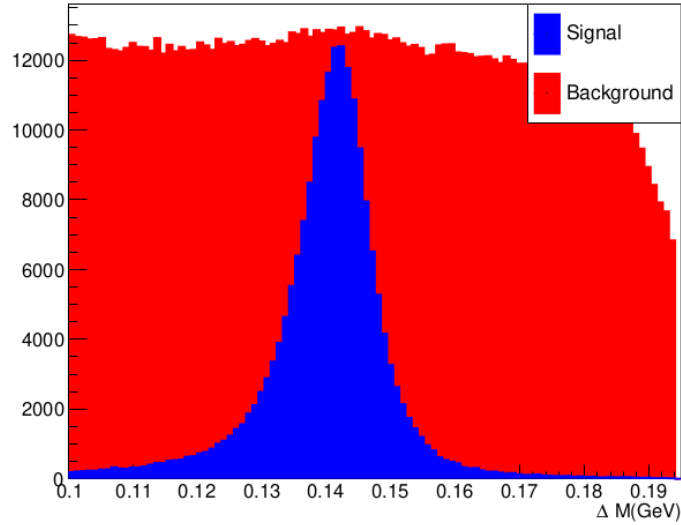


Figure 6.11:  $\Delta M$  after 1st optimisation

After applying the selection cut from the 1st optimisation on  $\gamma$  energy, we again plot the overlay of the other selected kinematic variables for optimisation to ensure whether they still behave to be good variables for optimisation. We do not find significant change in the overlay plots of the kinematic variables after the 1st optimisation. **Next we take the transverse momentum of  $\gamma$  as the variable for 2nd optimisation.**

We again find the figure of merit(FOM) plot for this respective kinematic variable and calculate the signal selection efficiency and the background selection efficiency. Then we choose a value for the  $\gamma$  transverse momentum for which we get high signal selection efficiency and low background selection efficiency, i.e., high background rejection efficiency similar to what we did in the previous case of  $\gamma$  energy.

In Figure-6.12, again  $\epsilon_s$  denotes the signal selection efficiency and  $\epsilon_b$  denotes the background selection efficiency. The background rejection efficiency is calculated by subtracting the background selection efficiency from 1. Looking at the signal selection values and background selection values from Figure-6.12 we see that for  $\gamma$  energy  $\geq 0.21$  GeV we get signal selection efficiency ( $\epsilon_s$ ) = 76% and background rejection efficiency ( $1 - \epsilon_b$ ) = 49%. The value of FOM is also high close to 0.44. Thus after the second optimisation the final selection cut on the transverse momentum of  $\gamma$  is  $\gamma_{pt} \geq 0.21$  GeV.

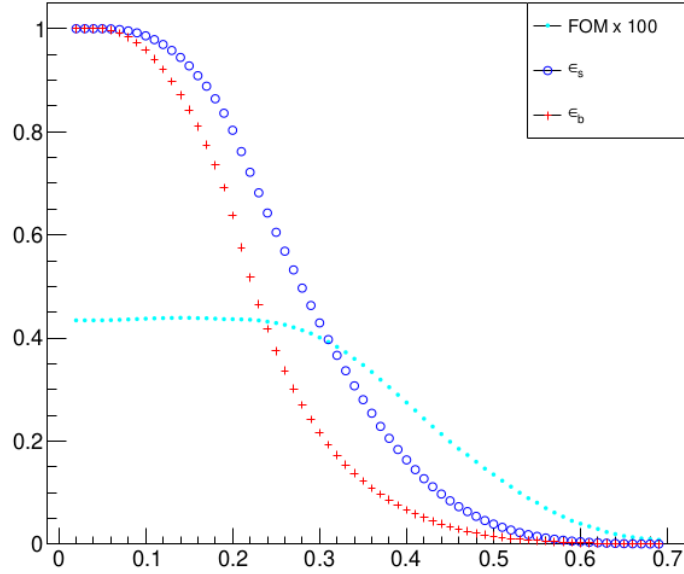


Figure 6.12: Figure of merit plot for  $\gamma$  transverse momentum

## 6.5 Third Optimisation

We also get the final selection cut on  $\gamma$  transverse momentum and we apply that cut along with the cut obtained from 1st optimisation and get the overlay distribution of  $\Delta M$ . Figure-6.13 shows the  $\Delta M$  overlay plot after the 2nd optimisation. We can see that compared to Figure-6.11, Figure-6.13 shows further lesser amount of background. Comparing with Figure-6.9, Figure-6.13 shows very much less amount of background. Infact the background height is now below that of the signal. Thus we can conclude that the selection cut obtained after the second optimisation has very good effect in reducing the background.

Now, total number of signal events before 1st optimisation, i.e., total number of signal events from reconstruction = 247155.

Number of signal events after 2nd optimisation = 130326.

Now applying Equation-6.1 the signal efficiency after 2nd optimisation is,

$$\eta = \frac{130326}{247155} \times 100\% = 52.73\%$$

Again we plot the overlay of the other selected kinematic variables, by applying the

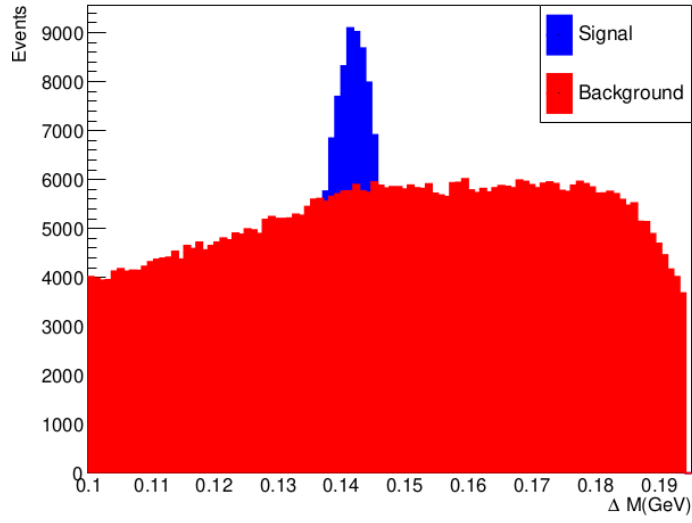
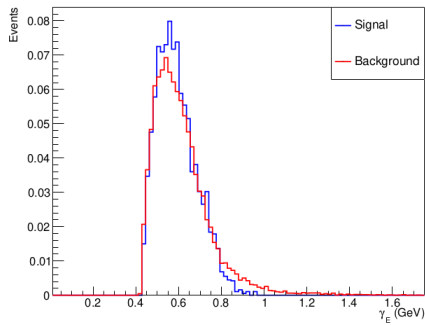
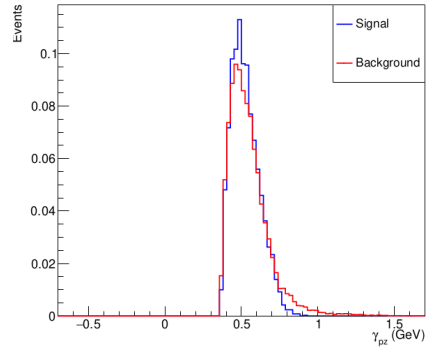


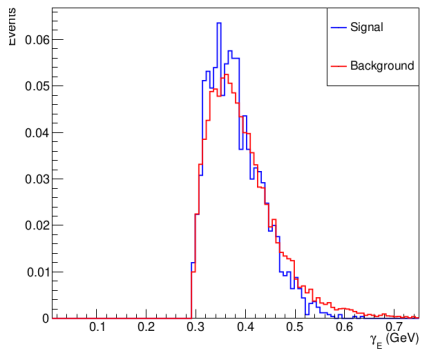
Figure 6.13:  $\Delta M$  after 2nd optimisation



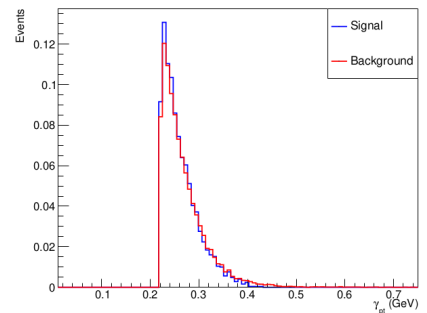
(a)  $\gamma$  energy in forward region



(b)  $\gamma$  transverse momentum in z-direction



(c)  $\gamma$  energy in backward region



(d)  $\gamma$  transverse momentum in backward region

Figure 6.14: Overlay plots of  $(\gamma)$  in forward and backward region after 2nd optimisation

selection cuts on  $\gamma$  energy and  $\gamma$  transverse momentum. We find that the kinematic variables of  $\gamma$  in the forward region( $\text{clusterReg}==1$ ) and backward region( $\text{clusterReg}==3$ ) now do not show good distinction between the signal and background distributions. Figure-6.14 shows the overlay plots of the kinematic variables of  $\gamma$  in the cluster regions 1 and 3 respectively. We can see that these overlay plots show similar nature of signal and background and they lay on top of each other. Thus these kinematic variables are no longer good choice for optimisation. **Thus our kinematic variable for 3rd optimisation is the energy of  $\gamma$  in the barrel region( $\text{clusterReg}==2$ ).**

We again find the figure of merit(FOM) plot for this respective kinematic variable and calculate the signal selection efficiency and the background selection efficiency.

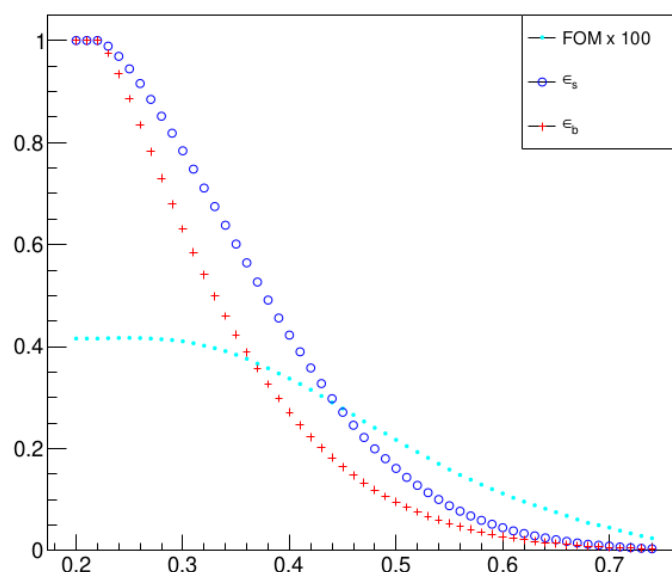


Figure 6.15: Figure of merit plot for  $\gamma$  energy in cluster region 2

In Figure-6.15, again  $\epsilon_s$  denotes the signal selection efficiency and  $\epsilon_b$  denotes the background selection efficiency. The background rejection efficiency is calculated by subtracting the background selection efficiency from 1. Looking at the signal selection values and background selection values from Figure-6.15 we see that in cluster region 2 for  $\gamma$  energy  $\geq 0.30$  GeV we get signal selection efficiency ( $\epsilon_s$ ) = 78% and background rejection efficiency ( $1 - \epsilon_b$ ) = 37%. The value of FOM is also high close to 0.41. Thus after the third optimisation the final selection cut on the energy of  $\gamma$  in  $\text{clusterReg}==2$  is  $\gamma_E^{\text{reg}2} \geq 0.30$  GeV.

## 6.6 Fourth Optimisation

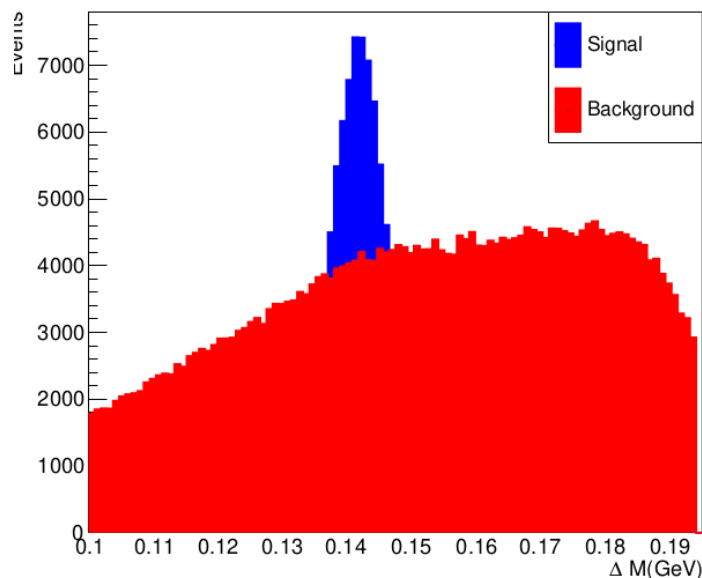


Figure 6.16:  $\Delta M$  after 3rd optimisation

We now get the final selection cut on  $\gamma$  energy in cluster region 2 and we apply that cut along with all the other cuts obtained from the previous optimisation. We get the overlay distribution of  $\Delta M$ . Figure-6.16 shows the  $\Delta M$  overlay plot after the 3rd optimisation. We can see that compared to Figure-6.13 and Figure-6.11, Figure-6.16 shows further lesser amount of background. Comparing with Figure-6.9, Figure-6.16 shows a drastic decrease in the amount of background. The background height is now well below that of the signal. Thus we conclude that the selection cut obtained after the third optimisation also has very good effect in reducing the background.

Now, total number of signal events from reconstruction = 247155.

Number of signal events after 3rd optimisation = 101358.

Now applying Equation-6.1 the signal efficiency after 3rd optimisation is,

$$\eta = \frac{101358}{247155} \times 100\% = 41\%$$

After applying the selection cut from the 3rd optimisation on  $\gamma$  energy in cluster region 2, we again plot the overlay of the selected kinematic variables which still showed distinction between the signal and background distribution for optimisation. This time we

do not find significant change in the overlay plots of the left kinematic variables after the 3rd optimisation, as we got after 2nd optimisation. **Next we take the transverse momentum of  $\gamma$  in the barrel region(clusterReg==2) as the variable for 4th optimisation.**

The figure of merit(FOM) plot for this respective kinematic variable is again plotted and the signal selection efficiency and the background selection efficiency are simultaneously calculated.

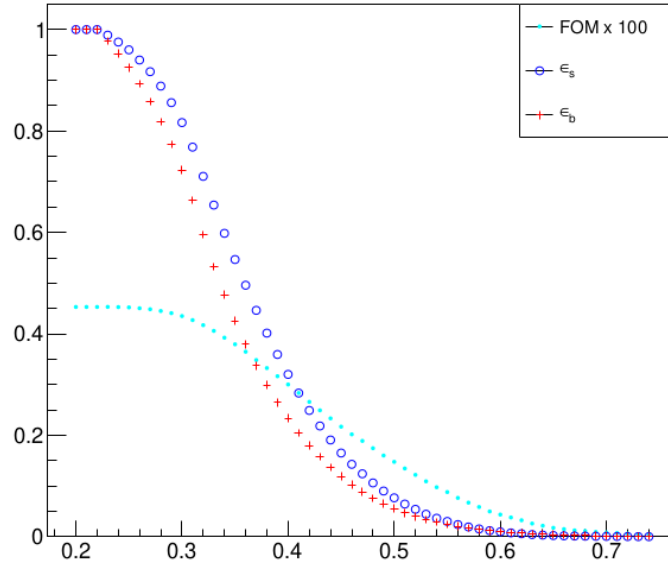


Figure 6.17: Figure of merit plot for  $\gamma$  transverse momentum in cluster region 2

In Figure-6.17, again  $\epsilon_s$  denotes the signal selection efficiency and  $\epsilon_b$  denotes the background selection efficiency. The background rejection efficiency is calculated by subtracting the background selection efficiency from 1. Looking at the signal selection values and background selection values from Figure-6.17 we see that in cluster region 2 for  $\gamma$  transverse momentum  $\geq 0.30$  GeV we get signal selection efficiency ( $\epsilon_s$ ) = 80% and background rejection efficiency ( $1 - \epsilon_b$ ) = 41%. The value of FOM is also high close to 0.41. Thus after the third optimisation the final selection cut on the transverse momentum of  $\gamma$  in clusterReg==2 is  $\gamma_{pt}^{reg2} \geq 0.26$  GeV.

## 6.7 Fifth Optimisation

We now get the final selection cut on  $\gamma$  transverse momentum in cluster region 2 also and we apply that cut along with all the other cuts obtained from the previous optimisation. We get the overlay distribution of  $\Delta M$ . Figure-6.18 shows the  $\Delta M$  overlay plot after the 4th optimisation. We can see that compared to Figure-6.16, Figure-6.18 shows little change in the decrease of background. However compared to Figure-6.13 and Figure-6.11, Figure-6.18 shows further lesser amount of background. Comparing with Figure-6.9, Figure-6.18 shows further drastic decrease in the amount of background. The background height is now well below that of the signal. Thus we conclude that the selection cut obtained after the fourth optimisation also has very good effect in reducing the background but it slowly is getting saturated and the background might not get reduced by a large amount in further optimisations.

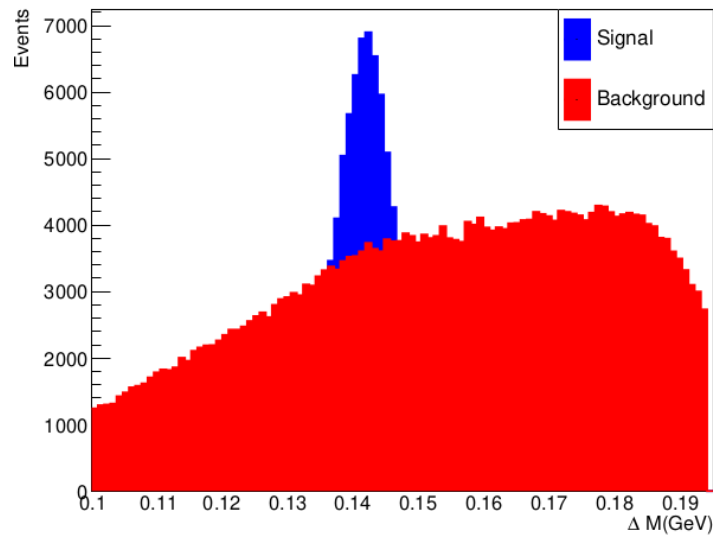


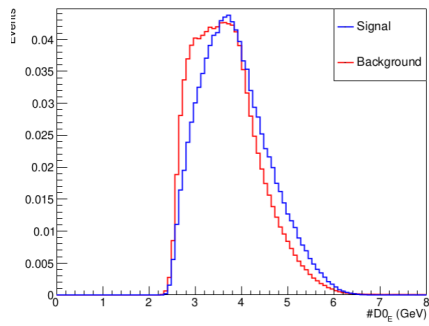
Figure 6.18:  $\Delta M$  after 4th optimisation

Now, total number of signal events from reconstruction = 247155.

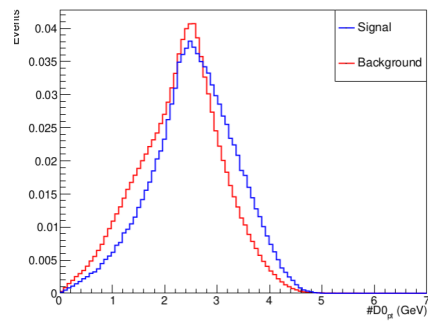
Number of signal events after 3rd optimisation = 92645.

Now applying Equation-6.1 the signal efficiency after 3rd optimisation is,

$$\eta = \frac{92645}{247155} \times 100\% = 37.48\%$$



(a) Overlay plot of  $D^0$  energy



(b) Overlay plot of  $D^0$  transverse momentum

Figure 6.19: Overlay plots of  $D^0$

Again we plot the overlay of selected kinematic variables which are left, by applying all the previous selection cuts. We find that the some of kinematic variables of  $D^0$  now do not show good distinction between the signal and background distributions. Figure-6.19 shows the overlay plots of the kinematic variables of  $D^0$ . We can see that the energy of  $D^0$  and the transverse momentum of  $D^0$  now show no significant difference between the distributions of signal and background. Thus these kinematic variables are no longer good choice for optimisation. **Thus our final kinematic variable with which we are left for 5th optimisation is the momentum of  $D^0$ .**

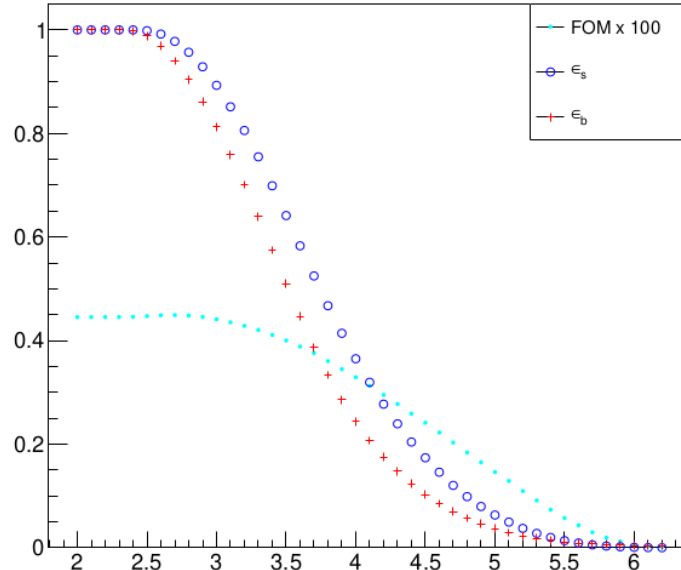


Figure 6.20: Figure of merit plot for  $D^0$  momentum

The figure of merit(FOM) plot for this respective kinematic variable is again plotted and the signal selection efficiency and the background selection efficiency are simultaneously calculated. In Figure-6.20, again  $\epsilon_s$  denotes the signal selection efficiency and  $\epsilon_b$  denotes the background selection efficiency. The background rejection efficiency is calculated by subtracting the background selection efficiency from 1. Looking at the signal selection values and background selection values from Figure-6.20 we see that for  $D^0$  momentum  $\geq 2.7 \text{ GeV}$  we get signal selection efficiency ( $\epsilon_s$ ) = 76% and background rejection efficiency ( $1 - \epsilon_b$ ) = 40%. The value of FOM is also high close to 0.42. Thus after the fifth and final optimisation the final selection cut on the momentum of  $D^0$  is  $D_p^0 \geq 2.7 \text{ GeV}$ .

## 6.8 Result after Optimisation

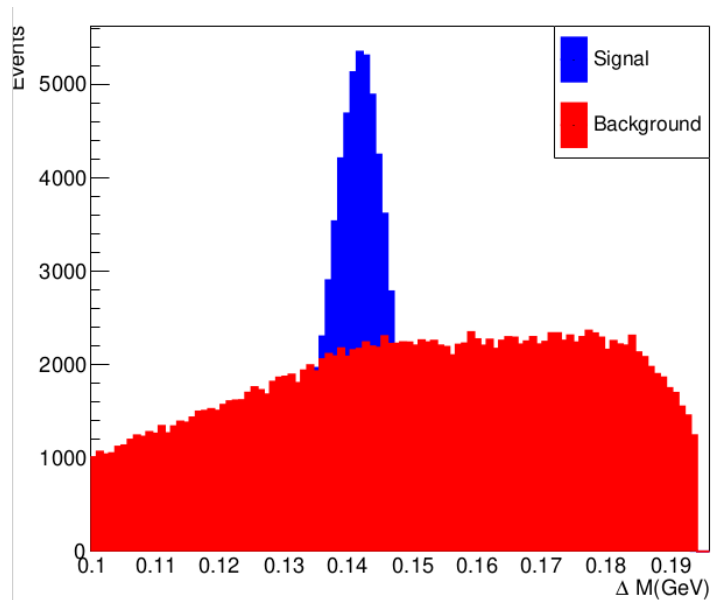


Figure 6.21:  $\Delta M$  after 5th optimisation

After applying the final selection cut on the momentum of  $D^0$  along with all the other previous cuts obtained during optimisation we get the final overlay plot of  $\Delta M$  as shown in Figure-6.21. Here we can clearly see that there is not much difference in the background if we compare it with Figure-6.18. From this we can conclude that our optimisation is over and the reduction of background has saturated. The background can no longer be decreased by significant amount by applying any other cuts. However if

we compare it with Figure-6.9 we can clearly see that the background has been reduced to a very great extent. The signal is now peaking very much above the background and is very much significant that what it was in Figure-6.9. Thus our optimisation is successful as we have been able to reduce the background very much without affecting the signal much. Now we use this distribution of  $\Delta M$  for fitting and yield calculation.

The final selection cuts along with the initial ones are listed in Table-6.1. While optimisation we saw that few variables which we chose at first during variable selection, while doing the N-1 optimisation, turned out to be not good variables for optimisation. From here we can conclude that all the variables we chose during variables selection were not independent of each other and hence they changed their overlay distribution as soon as the other dependent variable was optimised.

Objects	Pre-Selection Cuts	Final Selection Cuts
Tracks	$ drl  < 0.5 \text{ cm}$ and $ dzl  < 2 \text{ cm}$	$ drl  < 0.5 \text{ cm}$ and $ dzl  < 2 \text{ cm}$
$K^+$	KaonID $\frac{\mathcal{L}_K}{\mathcal{L}_K + \mathcal{L}_\pi} > 0.3$	KaonID $\frac{\mathcal{L}_K}{\mathcal{L}_K + \mathcal{L}_\pi} > 0.3$
$\pi^+$	PionID $\frac{\mathcal{L}_\pi}{\mathcal{L}_K + \mathcal{L}_\pi} > 0.3$	PionID $\frac{\mathcal{L}_\pi}{\mathcal{L}_K + \mathcal{L}_\pi} > 0.3$
$D^0$	$1.8148 < M(K^- \pi^+) < 1.9148 \text{ GeV}/c^2$	$1.8148 < M(K^- \pi^+) < 1.9148 \text{ GeV}/c^2$ $D_p^0 \geq 2.7 \text{ GeV}$
$\gamma$	$\gamma_E^{barrel} > 30 \text{ MeV}$ $\gamma_E^{forward} > 120 \text{ MeV}$ $\gamma_E^{backward} > 80 \text{ MeV}$	$\gamma_E^{barrel} > 300 \text{ MeV}$ $\gamma_{pt}^{barrel} > 260 \text{ MeV}$ $\gamma_E^{forward} > 120 \text{ MeV}$ $\gamma_E^{backward} > 80 \text{ MeV}$ $\gamma_E > 130 \text{ MeV}$
$D_s^{*+}$	$2.06 < M(D_s^+ \gamma) < 2.16 \text{ GeV}/c^2$ $0.06 < \Delta M < 0.2 \text{ GeV}/c^2$	$2.06 < M(D_s^+ \gamma) < 2.16 \text{ GeV}/c^2$ $0.06 < \Delta M < 0.2 \text{ GeV}/c^2$

Table 6.1: Table for Selection Cuts

Thus the final list of variables used for optimisation listed are :

1.  $\gamma$  energy
2.  $\gamma$  transverse momentum
3.  $\gamma$  energy(in clusterReg==2)
4.  $\gamma$  transverse momentum(in clusterReg==2)
5.  $D^0$  momentum

# Chapter 7

## Fitting of $\Delta M$ after optimisation

We now have the overlay plot of  $\Delta M$  with the signal and background distribution. This overlay plot as shown in Figure-6.21 is the final optimised distribution containing all the selection cuts we got during optimisation. Now we have to fit the distributions properly with appropriate functions so as to calculate the mean, standard deviation and yield from the distribution. The fitting is done by a software package pre-installed in ROOT called RooFit. The mean obtained from the total fit is then compared with the theoretically observed value of  $\Delta M$ . If the mean matches with that of the theoretical value, then we can finally conclude that our reconstruction of the decay channel is correct and we have successfully reconstructed  $D^{*0}$  from the channel under study.

### 7.1 Signal Fitting

At first we separate the signal and background from the total distribution of  $\Delta M$ . Then we convert the signal distribution into data points and plot them in a canvas. Figure-7.1 shows the plot of the data points of the signal of  $\Delta M$  after optimisation. Now with the help of RooFit we fit these data points using suitable function pdf.

After fitting we also plot the pull plot and calculate the  $\chi^2$  degree of freedom ( $\chi^2$  dof) which shows us the accuracy of the fit. Ideally the value of  $\chi^2$  dof should be equal to 1. However in practice a range of 0.5 to 2.0 is allowed for  $\chi^2$  dof. The pull of the fit must lie between  $\pm 3$ . The pull and  $\chi^2$  dof ensure that the pdf fitting the data points fits it very well and can be used for calculation of different parameters.

Figure-7.2 shows the pdf used to fit the signal distribution of  $\Delta M$ . Here we have used two functions and added them to produce a combined pdf for fitting the signal. The pull plot of the fit is also shown below and it shows that the pull is within  $\pm 3$ . From Figure-7.2 the value of  $\chi^2$  dof = 1.22. Thus the value of  $\chi^2$  dof is close to 1 and

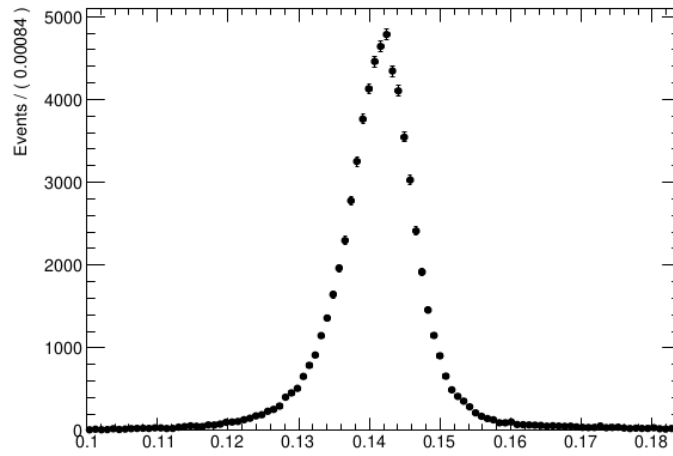


Figure 7.1: Data points of  $\Delta M$  signal

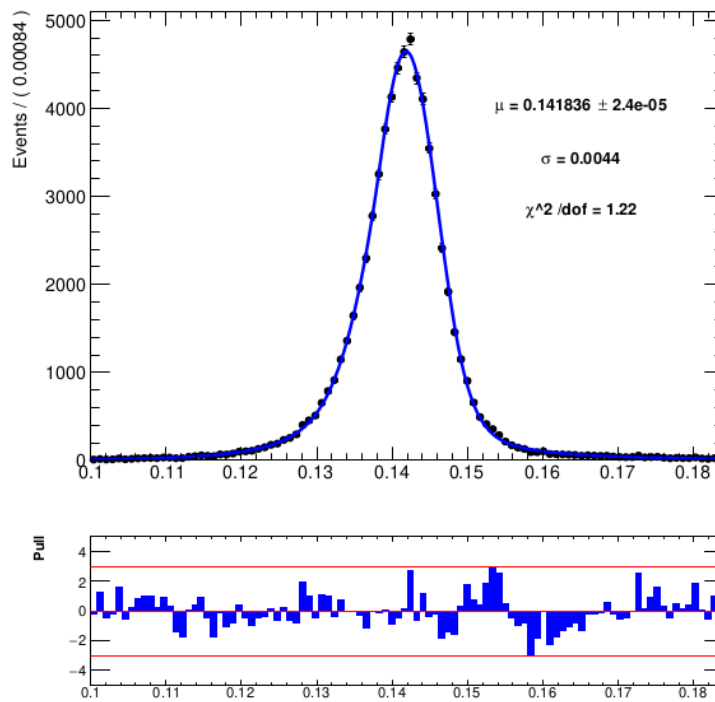


Figure 7.2: Fitting of  $\Delta M$  signal

the pull also lies within  $\pm 3$  so we conclude that the fit is a good one to the signal. We can also see that the mean is 0.142 which is in very good agreement with the theoretical value. This indicates the correctness and accuracy of the fit.

Generally a gaussian is used to fit the signal, but in our case the gaussian does not properly fit the signal data points as there are few data points forming a tail and hence gaussian fails to fit that part. Thus we use a **double crystal ball(DCB)** to fit the signal data points.

### 7.1.1 Crystal Ball Function

The Crystal Ball function is named after the Crystal Ball Collaboration. It is a probability density function(pdf) which is widely used for modelling various processes in high-energy physics. It consists of a Gaussian core portion and a power-law low-end tail, below a certain threshold. The function itself and its first derivative are both continuous. The mathematical form of the function is given as:

$$f(x; \alpha, n, \bar{x}, \sigma) = N \cdot \exp\left(-\frac{(x-\bar{x})^2}{2\sigma^2}\right) \quad \text{for } \frac{x-\bar{x}}{\sigma} > -\alpha \quad (7.1)$$

$$= N \cdot A \cdot \left(B - \frac{(x-\bar{x})^2}{2\sigma^2}\right) \quad \text{for } \frac{x-\bar{x}}{\sigma} \leq -\alpha \quad (7.2)$$

where

$$A = \left(\frac{n}{|\alpha|}\right)^n \cdot \exp\left(-\frac{|\alpha|^2}{2}\right)$$

$$B = \frac{n}{|\alpha|} - |\alpha|$$

$$C = \frac{n}{|\alpha|} \cdot \frac{1}{n-1} \cdot \exp\left(-\frac{|\alpha|^2}{2}\right)$$

$$D = \sqrt{\frac{\pi}{2}} \left(1 + \text{erf}\left(\frac{|\alpha|}{\sqrt{2}}\right)\right)$$

$$N = \frac{1}{\sigma(C+D)}$$

N is a normalization factor and  $\alpha, n, \bar{x}$  and  $\sigma$  are parameters which are fitted with the data. *erf* is the error function.

## 7.2 Background Fitting

After fitting the signal, we follow the same procedure for fitting the background. First we convert the background distribution into data points and plot them in canvas as shown

in Figure-7.3. Now with the help of RooFit we fit these data points using a threshold function p.d.f.

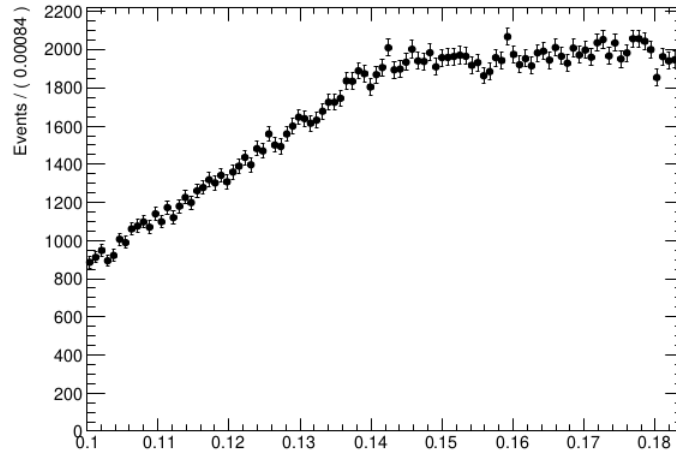


Figure 7.3: Data points of  $\Delta M$  background

After fitting we also plot the pull plot and calculate the  $\chi^2$  degree of freedom ( $\chi^2$  dof) which shows us the accuracy of the fit. Ideally the value of  $\chi^2$  dof should be equal to 1. However in practice a range of 0.5 to 2.0 is allowed for  $\chi^2$  dof. The pull of the fit must lie between  $\pm 3$ . The pull and  $\chi^2$  dof ensure that the pdf fitting the data points fits it very well and the pdf can be used for calculation of different parameters.

Figure-7.4 shows the pdf used to fit the background distribution of  $\Delta M$ . The pull plot of the fit is also shown below and it shows that the pull is within  $\pm 3$  except for one place which can be neglected considering that all the other points lies within the range. From Figure-7.4 the value of  $\chi^2$  dof = 1.51. Thus the value of  $\chi^2$  dof is close to 1 and the pull also lies within  $\pm 3$  so we conclude that the fit is a good one to the background.

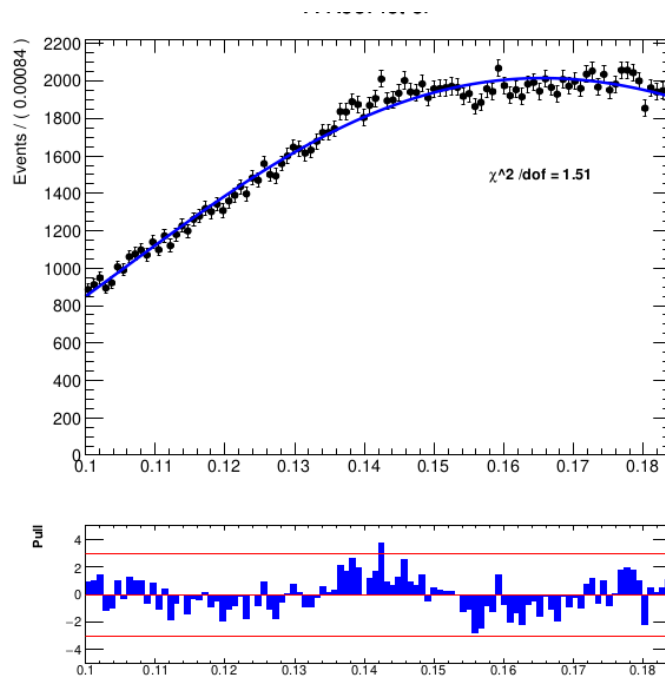


Figure 7.4: Fitting of  $\Delta M$  background

### 7.3 Total Fitting

Now after getting the signal fit and the background fit and the corresponding parameters, we can now do the fitting of the total distribution including the signal and the background. For this again we convert the distribution to data points first and plot them in a canvas as shown in Figure-7.5 Now we fit the total distribution data points with the combination of the p.d.f.s that we have obtained from the fitting of the signal and background separately. Thus we add the p.d.f.s of 'double crystal ball'(DCB) with that of the 'threshold function'.

After adding the p.d.f.s we fit it with our distribution data points for  $\Delta M$  and get the final fit for  $\Delta M$ . After fitting we also plot the pull plot and calculate the  $\chi^2$  degree of freedom( $\chi^2$  dof) which shows us the accuracy of the fit. Ideally the value of  $\chi^2$  dof should be equal to 1. However in practice a range of 0.5 to 2.0 is allowed for  $\chi^2$  dof. The pull of the fit must lie between  $\pm 3$ . The pull and  $\chi^2$  dof ensure that the pdf fitting the data points fits it very well and the pdf can be used for calculation of different parameters. We also calculate the mean( $\mu$ ), standard deviation( $\sigma$ ) and the total signal yield(N). Figure-7.6 shows the fit of the total distribution of  $\Delta M$ . We see that the pull is well within  $\pm 3$  and the value of  $\chi^2$  dof = 1.28. Thus the value of  $\chi^2$  dof is close to

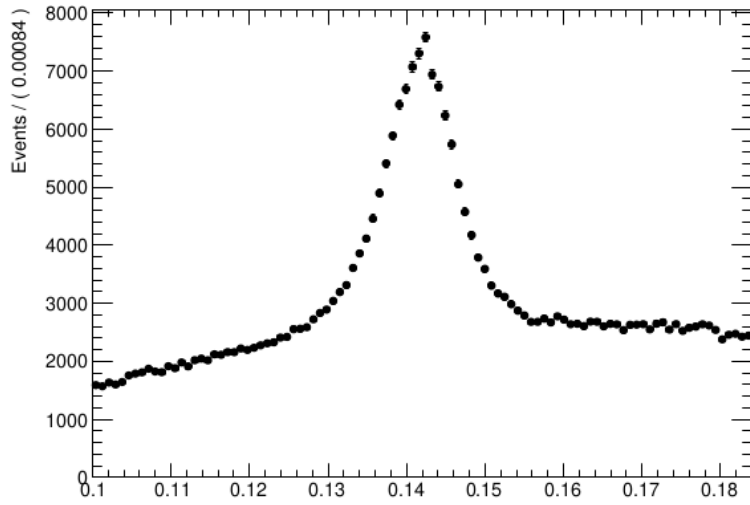


Figure 7.5: Data Points of  $\Delta M$

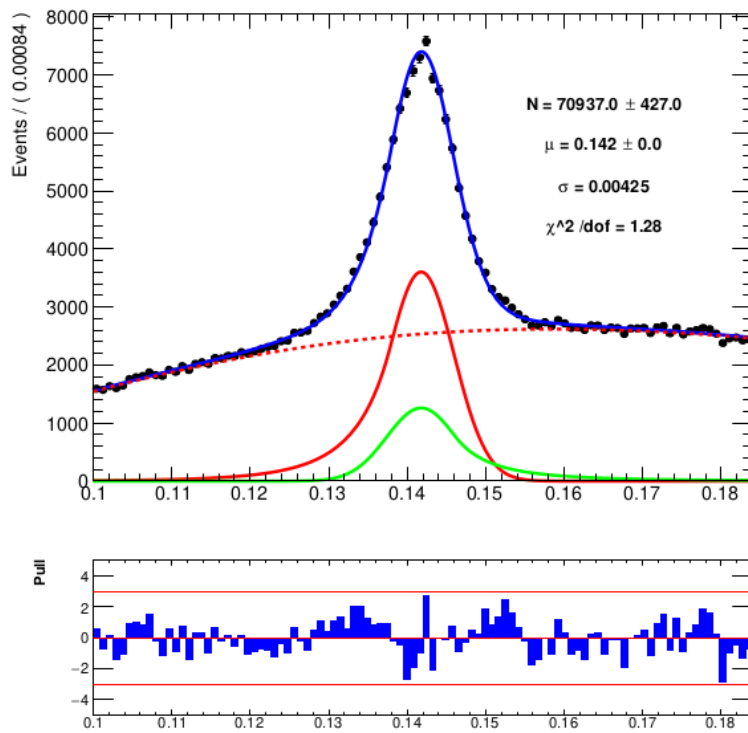


Figure 7.6: Fitting of  $\Delta M$

1 and the pull also lies within  $\pm 3$  so we conclude that the fit is a good one to the total distribution of  $\Delta M$ . The signal yield gives us the total value of events that is actually forming our decay channel under study. It is a very important parameter for the calculation of the Branching Ratio. From Figure-7.6 we can see that after fitting the mean( $\mu$ ) = 0.142 GeV which is exactly similar to the theoretical value of  $\Delta M$ . The value of the signal yield N is also of the same order from that of previous analysis.

Thus we conclude that our fit is correct and we have successfully reconstructed the charmed meson  $D^{*0}$  from the decay path  $D^{*0} \rightarrow D^0 \gamma, D^0 \rightarrow K^- \pi^+$  which we wanted to study.

# Bibliography

- [1] B. Aubert *et al.* [BaBar], *Phys. Rev. D* **72** (2005), 091101 /*PhysRevD.72.091101* [arXiv:hep-ex/0508039 [hep-ex]].
- [2] J. Gronberg *et al.* [CLEO], *Phys. Rev. Lett.* **75** (1995), 3232-3236 /*Phys-RevLett.75.3232* [arXiv:hep-ex/9508001 [hep-ex]].
- [3] Dickopp, M. Measurement of the partial widths ratio  $\Gamma(D(s)^*+ \rightarrow D(s)+\pi^0)/\Gamma(D(s)^*+ \rightarrow D(s)+\gamma)$  at the BABAR experiment. (? ,2004,4)
- [4] Goity, J. & Roberts, W. Radiative transitions in heavy mesons in a relativistic quark model. *Phys. Rev. D*.
- [5] Link, J., Reyes, M., Yager, P., Anjos, J., Bediaga, I., Göbel, C., Magnin, J., Massafferri, A., Miranda, J., Pepe, I. & Others New measurements of the  $D^0$  and  $D^+$  lifetimes. *Physics Letters B*. **537**, 192-200 (2002)
- [6] Ablikim, M., Achasov, M., Ai, X., Albayrak, O., Albrecht, M., Ambrose, D., Amoroso, A., An, F., An, Q., Bai, J. & Others Precision measurement of the  $D^*0$  decay branching fractions. *Physical Review D*. **91**, 031101 (2015)
- [7] Cronin-Hennessy, D., Gao, K., Hietala, J., Kubota, Y., Klein, T., Lang, B., Poling, R., Scott, A., Zweber, P., Dobbs, S. & Others Measurement of charm production cross sections in  $e^+e^-$  annihilation at energies between 3.97 and 4.26 GeV. *Physical Review D*. **80**, 072001 (2009)
- [8] Butler, F., Fu, X., Kalbfleisch, G., Lambrecht, M., Ross, W., Skubic, P., Snow, J., Wang, P., Bortoletto, D., Brown, D. & Others Measurement of the  $D^*(2010)$  branching fractions. *Physical Review Letters*. **69**, 2041 (1992)
- [9] Albrecht, H., Ehrlichmann, H., Hamacher, T., Hofmann, R., Kirchhoff, T., Mankel, R., Nau, A., Nowak, S., Rensing, D., Schröder, H. & Others Measurement of the decay fractions of  $D^*$  mesons. *Zeitschrift Für Physik C Particles And Fields*. **66**, 63-70 (1995)

- [10] Zyla, P. & Others Review of Particle Physics. *PTEP.* **2020**, 083C01 (2020), and 2021 update
- [11] Ono, S. Electromagnetic mass differences and decay rates of charmed mesons in the charmed-quark model. *Physical Review Letters.* **37**, 655 (1976)
- [12] Steven H. Robertson 2019 J. Phys.: Conf. Ser. 1271 012011.
- [13] Belle II Software Documentation.
- [14] The LHCb collaboration., Aaij, R., Abellán Beteta, C. et al. J. High Energ. Phys. 2019, 176 (2019)/JHEP03(2019)176
- [15] Brun, R., Rademakers, F., Panacek, S., Antcheva, I. & Buskulic, D. The ROOT Users Guide. *CERN, Http://root. Cern. Ch.* (2003)
- [16] Griffiths, D. Introduction to elementary particles. (John Wiley & Sons,2020)
- [17] Verkerke, W. & Kirkby, D. RooFit users manual v2. 91. (2011)